Clouds, Circulation, and Climate Sensitivity in a Radiative-Convective Equilibrium Channel Model

Timothy W. Cronin[1], **Allison A. Wing** [2,3]

[1]Department of Earth, Atmospheric, and Planetary Science, MIT, Cambridge, MA
[2]Lamont-Doherty Earth Observatory, Columbia University, Palisades, NY
[3]Department of Earth, Ocean and Atmospheric Science, Florida State University, Tallahassee, FL

Key Points:

- Channel RCE simulations generate realistic tropical dynamical regimes that weaken with warming
- Anvil clouds shift up and decrease in response to warming, with or without convective aggregation
- The cloud feedback on warming is positive and aggregation modestly reduces climate sensitivity

Corresponding author: Timothy W. Cronin, twcronin@mit.edu

Abstract

Tropical cloud and circulation changes are large sources of uncertainty in future climate change. This problem owes partly to the scale separation between large-scale tropical dynamics ($\sim 10^4$ km) and convective dynamics (~ 1 km), which generally requires parameterizing convection in models that resolve large-scale dynamics, or parameterizing (or omitting) large-scale dynamics in models that permit convection. Here we discuss simulations of radiative-convective equilibrium (RCE) across a wide range of surface temperatures in long channel geometry – where the domain size and resolution marginally resolve both large-scale dynamics and convection. Self-aggregation of convection in these simulations spontaneously produces realistic dynamical regimes of large-scale vertical motion. The circulation weakens with surface warming but changes in the degree of self-aggregation depend on the metric that is used; there is no obvious trend in aggregation with warming. Surface warming causes an upward shift and decrease in area of high clouds, and a sharp decline in mid-level clouds, but no systematic trend in low cloud cover. We introduce a method for approximate radiative kernel feedback analysis in RCE, and apply it to both simulations in long channel geometry and in a smaller square domain. The kernel-corrected cloud feedback is positive but its magnitude varies across temperatures. Compared to simulations that do not have aggregation, there is a more negative net feedback due to the effects of aggregation on relative humidity and cloud cover. These results are consistent with the hypothesis that self-aggregation moderately reduces climate sensitivity.

1 Introduction

The response of clouds to climate warming remains one of the largest sources of uncertainty in understanding the response of Earth's climate to altered CO_2, solar forcing, or other climate drivers [e.g., *Bony et al.*, 2015; *Sherwood et al.*, 2014; *Zelinka and Hartmann*, 2012]. One major barrier to understanding how clouds change with warming is that the tropical cloud response – critical to the sign and magnitude of the overall radiative cloud feedback – is mediated by convection, which occurs mostly at scales much smaller than the grid cells in General Circulation Models (GCMs). Although global or near-global convection-permitting simulations like those of *Satoh et al.* [2008] and *Bretherton and Khairoutdinov* [2015] – which have grid spacing fine enough to marginally resolve deep convection – represent one promising way to overcome this barrier, they remain too computationally expensive to use for long simulations over a wide range of climates. Use of convection-permitting models in small domains has helped address many questions in recent years about how convection and rainfall extremes are likely to change with warming [e.g., *Muller et al.*, 2011; *Romps*, 2011; *Muller*, 2013; *Singh and O'Gorman*, 2013, 2014, 2015; *Romps*, 2014; *Seeley and Romps*, 2015, 2016]. Such simulations, however, can only peripherally address questions about changes in clouds and relative humidity, because these changes are linked to large-scale circulations, which may also change with warming [e.g., *Bony et al.*, 2015, 2004]. Convection-permitting models in small domains must either prescribe, parameterize, or neglect changes in large-scale circulation; the latter is most common as it follows from the basic-state assumption of radiative-convective equilibrium (RCE), whereby the domain as a whole is subject to no large-scale heat, moisture, or momentum convergence.

Although long unexplored, RCE in GCMs (with parameterized convection) has recently emerged as a potentially valuable tool for understanding convective aggregation and climate feedbacks. As noted by *Held et al.* [2007], even though RCE in a global model theoretically has a solution where all columns remain identical to one another, with equal convection at all times and in all grid cells, this solution is apparently unstable to development of large-scale circulation, leading to spatial heterogeneity in convection and rainfall. Further work has upheld this general finding, and has taken advantage of the spatial heterogeneity of RCE in GCMs to study climate sensitivity [*Popke et al.*, 2013; *Becker and Stevens*, 2014], changes in anvil clouds with warming [*Bony et al.*, 2016], sensitivity of precipitation extremes to warming [*Pendergrass et al.*, 2016], and the influence of model configuration – including resolution,

domain size, and convection scheme – on the aggregation of convection and the properties of the climate in RCE [*Reed et al.*, 2015; *Silvers et al.*, 2016; *Becker et al.*, 2017]. Although examining RCE with GCMs has yielded insight on climate and climate sensitivity, such studies remain clouded by the same structural uncertainties about role of subgrid-scale physics – particularly in the convective parameterization – that are present in all global models used to project future climate.

In this paper, we attempt to partly bridge the gap between small-domain convection-permitting models, and RCE in GCMs with parameterized convection, by using a long-channel model geometry with a convection-permitting model [as in *Wing and Cronin*, 2016], in which large-scale circulations develop spontaneously in a dynamic RCE state. These large-scale circulations are associated with self-aggregation of convection, or the spontaneous and persistent organization of convection despite homogeneous boundary conditions and forcing. Self-aggregation has been found to occur in RCE simulations in a variety of models using either explicit or parameterized convection [*Wing et al.*, 2017, and references therein] and has also been hypothesized as important for climate and climate sensitivity [*Khairoutdinov and Emanuel*, 2010; *Bony et al.*, 2015; *Mauritsen and Stevens*, 2015]. Motivated by the finding that the channel RCE simulations show a similar distribution of large-scale dynamical regimes to the real tropics, and by the World Climate Research Programme (WCRP) grand challenge on "Clouds, Circulation, and Climate Sensitivity" [*Bony et al.*, 2015], we analyze the clouds, circulation, and climate sensitivity in these simulations across a wide range of surface temperatures.

We first describe the simulations and compare the modeled large-scale circulation in dynamical regime space to the real tropical atmosphere (section 1.1). The paper is then organized in three main sections – respectively on degree of aggregation and circulation (section 2), clouds (section 3), and climate sensitivity (section 4) – each of which contains background and description of analysis methods used therein. In section 2, we present two metrics of the degree of aggregation of convection and how they depend on surface temperature, then use a simple scaling to understand changes in the overturning circulation with warming. We next analyze changes in clouds with warming (section 3). Finally, we estimate climate feedbacks (section 4) using a new, computationally efficient, approximate kernel method for calculating radiative feedbacks in RCE (Appendix B). Overall, we believe that the combination of realistic large-scale dynamical regimes and resolved deep convection in the long-channel RCE model configuration offers new possibilities for assessing tropical cloud and circulation feedbacks under climate change.

1.1 Channel simulations of RCE

We simulate non-rotating radiative-convective equilibrium (RCE) with version 6.8.2 of the System for Atmospheric Modeling (SAM, *Khairoutdinov and Randall* [2003]) in three-dimensional elongated channel geometry. The domain has dimensions of 12,288 km $\times$ 192 km in the horizontal, with a resolution of 3 km and doubly-periodic lateral boundaries. The simulations are performed over a wide range of temperatures with fixed, uniform, sea-surface temperature (T_S) between T_S = 280 K and T_S = 310 K, in 5 K increments. Most of the simulations have 64 vertical levels on a stretched vertical grid with a rigid lid at 28 km and a sponge layer in the upper third in the domain, but the simulation at T_S = 310 K has 74 vertical levels with a model top at 33 km, to ensure the sponge layer does not impede the convection. The longwave and shortwave radiative heating rates are calculated interactively using the RRTMG radiation scheme [*Clough et al.*, 2005; *Iacono et al.*, 2008; *Mlawer et al.*, 1997], and we use a diurnal cycle of insolation at 19.45 N at perpetual Julian day 80.5 (which yields a time-mean insolation of 413.6 Wm^{-2}, close to the tropical annual mean value). As in *Wing and Cronin* [2016], the SAM one-moment microphysics parameterization is used. The major differences from the experimental design in *Wing and Cronin* [2016] are that: 1) this work uses the RRTMG rather than the CAM radiation scheme, and 2) the vertical extent of the domain is extended for $T_S = 310$ K.

The channel simulations are run for 75 days and a small amount of initial white noise in the boundary layer temperature field is imposed so that convection develops quickly. The simulations are initialized with an average sounding from a small-domain simulation of RCE (96 km $\times$ 96 km in the horizontal, with 1 km resolution) that uses the same boundary conditions. These small-domain simulations do not generate organized convection or large-scale circulations, so we additionally use them as a control that represents the response of "conventional" RCE to warming.

Across all temperatures, the convection in the channel simulations spontaneously organizes into multiple convectively active and suppressed regions, which appear as alternating moist and dry bands of O(1000 km) in scale (Figure 1). Each convectively active region has mean ascent, while there is large-scale subsidence in the dry areas, with overturning circulations between moist and dry regions. The process of self-aggregation in the channel simulations, including its growth rates, physical mechanisms, and length scales, are described in *Wing and Cronin* [2016].

Since this paper will not explore in depth the distribution of precipitation rates or their changes with warming, changes in the hydrological cycle are summarized here. Over the whole temperature range, mean and extreme precipitation rates both increase with warming, but extreme rates increase faster. Mean precipitation in the channel simulations increases at an average of 3.9 $\%^{\circ}\mathrm{C}^{-1}$, a larger rate than in some GCMs because our warming is forced by sea-surface temperature increases without changes in CO_2 [e.g., *Allen and Ingram*, 2002]. Extreme precipitation, quantified as the 99.9 percentile of daily rainfall, increases at an average of 6.5 $\%^{\circ}\mathrm{C}^{-1}$ (calculating percentiles over both rainy and dry grid cells). This result is close to Clausius-Clapeyron scaling, as found in *Singh and O'Gorman* [2014]. The more rapid increase in extreme than mean rainfall rates suggests a decrease in the fraction of rainy grid cells with warming; this fraction does indeed decrease sharply between 280-295 K from about 0.3 to 0.15, but then remains close to 0.15 for higher surface temperatures – indicating that more subtle changes in the shape of the probability density function of precipitation rate may take place at higher temperatures. Mean precipitation in the small domain simulations (without aggregation) is about 23% less than in the aggregated channel simulations, but increases at about the same rate with warming. Extreme rainfall in the small domain simulations increases at an average of 6.0 $\%^{\circ}\mathrm{C}^{-1}$, which is not significantly different from the increase with warming in the channel simulations. Detailed investigation of the factors that control the whole rainfall rate distribution in these simulations, and its dependence on surface temperature, is left as a subject for future work.

1.2 Comparison of channel RCE and tropical atmosphere

Self-aggregation of convection in the channel simulations spontaneously generates large scale circulations that can be quantified as "dynamical regimes", following *Bony et al.* [2004]. We compute the probability density function P_ω of block-averaged 500-hPa vertical velocity over 5- and 10- day periods within days 25-75 of the channel simulation at T_S = 300 K, which is close to current tropical sea-surface temperatures. We use 192 km $\times$ 192 km blocks, roughly equivalent to a 1.75-degree grid. These dynamical regimes of large-scale vertical motion compare well to those of the real tropical atmosphere (Figure 2). Notable discrepancies are that the strongest subsidence in our simulation is weaker than in the real tropics, that the peaks of the distributions do not match exactly, and that our P_ω is sensitive to choice of averaging period. The missing strong subsidence – or fall-off of our P_ω at 40 hPa d^{-1} – is likely connected to our lack of SST gradients, topography, and stratocumulus. The mismatch of peaks is likely also tied to the lack of a strong subsidence regime. Finally, the sensitivity to averaging period is expected with homogeneous boundary conditions, since we expect that P_ω should tighten towards a peak at $\omega = 0$ on time scales long enough to allow for migration of moist and dry regions.

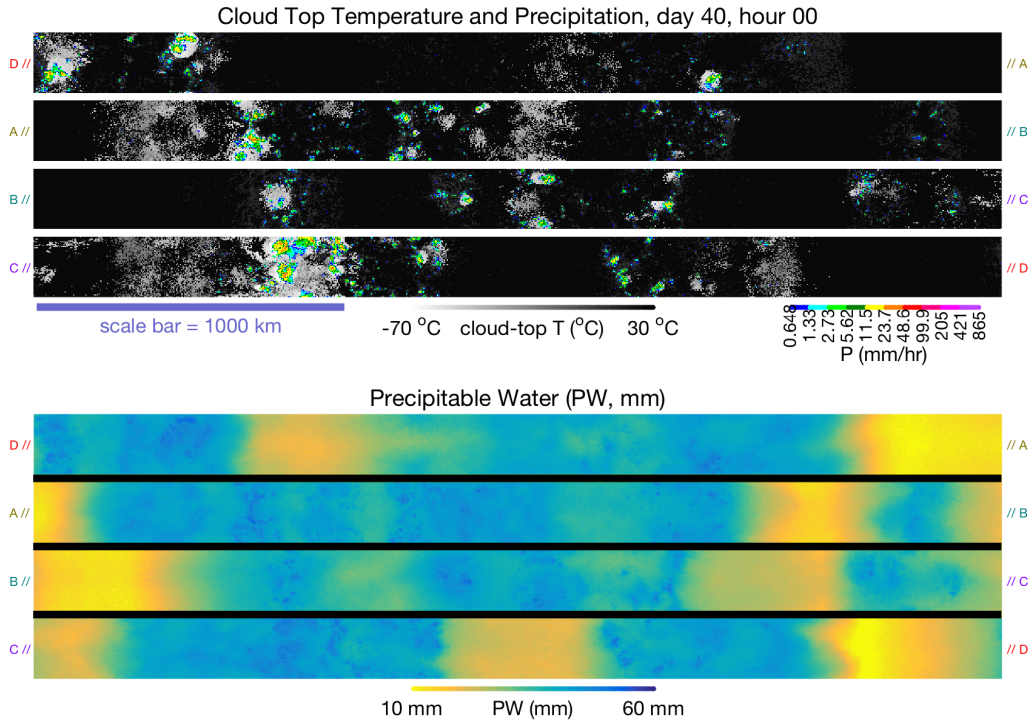

Figure 1. Snapshot of convection in channel simulation at T_S = 300 K. The top subplot shows the cloud top temperature and precipitation rate while the bottom subplot shows the precipitable water. For ease of visualization, the channel is divided into quarters and each segment is wrapped left-to-right, as if it were lines of text.

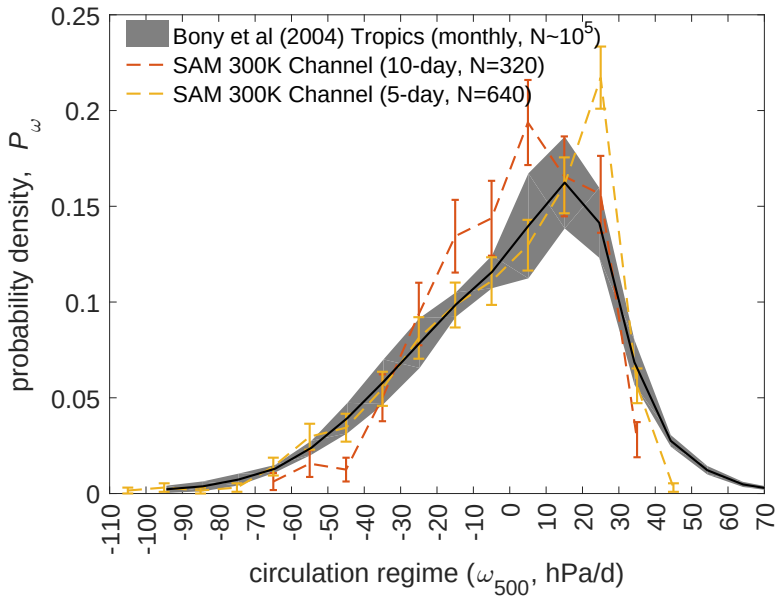

Figure 2. Solid black line: Mean large-scale monthly 500-hPa vertical velocity in Tropics (30S to 30N) on 2.5 $\times$ 2.5 degree grid, years 1987-1988 across three reanalysis datasets; gray shading indicates standard deviation across three datasets [*Bony et al.*, 2004]. Dashed colors: block-averaged (192 $\times$ 192 km, roughly equivalent to a 1.75-degree grid) 500-hPa vertical velocity over 5- and 10-day periods, days 25-75 of the SAM channel simulation at 300 K. Error bars for SAM are determined as standard deviations of P_ω in each bin from 10000 bootstrapped resamples of the block-averaged ω_{500} data.

Self-aggregation also generates significant humidity variability in the channel simulations; water vapor mixing ratio and relative humidity are substantially reduced in the dry, non-convecting regions relative to the moist, convecting regions at all levels, but especially in the mid-troposphere. *Holloway et al.* [2017] compared this *spatial* humidity variability in a channel RCE simulation to observed *temporal* humidity variability from five years of twice-daily radiosondes at the Nauru ARM site in the Pacific warm pool. They found that the mixing ratio and relative humidity profiles in dry and moist subsets of sondes were similar to the equivalent dry and moist profiles in the channel simulation. *Holloway et al.* [2017] also found that the statistics of near surface relative humidity variability were similar between the Nauru station and the channel simulation. We do not claim that the humidity variability at the Nauru station is generated by the same mechanisms as in our simulations of self-aggregation, but the results of *Holloway et al.* [2017] nevertheless suggest that the range of humidity values in the channel simulation is reasonable. This also supports the use of channel simulations for assessing non-cloud radiative feedbacks on warming (discussed in section 4).

Reasonable large-scale circulation regimes and humidity variability in the channel RCE configuration due to self-aggregation indicate that this model configuration may be valuable for learning about clouds, circulation, and climate sensitivity. The channel simulation shown may, of course, obtain the "right" answer for the "wrong" reasons. Many of the phenomena or processes that generate circulations and humidity variability in the real Tropics are absent in these simulations, such as equatorial Rossby and inertio-gravity waves, coupled air-sea phenomena, tropical landmasses and topography, and transport of air from mid-latitudes. Despite these missing processes, we find the similarities between our simulations and the tropical atmosphere striking enough to merit serious analysis and study. If the reader remains skeptical about the application of any of our results to the real Tropics, then this paper can nonetheless be read through the lens of the question: "How does self-aggregation of convection – in a hypothetical tropical atmosphere dominated by this phenomenon – affect the sensitivity of clouds, circulation, and top-of-atmosphere radiative fluxes to warming?"

2 Degree of aggregation and circulation changes

The most dramatic way that self-aggregation has been hypothesized to play a role in climate is via strong temperature-dependence, combined with a large change in net top-of-atmosphere radiative fluxes between aggregated and non-aggregated states [*Khairoutdinov and Emanuel*, 2010; *Mauritsen and Stevens*, 2015]. Several numerical modeling studies have indeed found that self-aggregation is favored at high temperatures [*Held et al.*, 1993; *Khairoutdinov and Emanuel*, 2010; *Wing and Emanuel*, 2014; *Emanuel et al.*, 2014; *Coppin and Bony*, 2015], especially in square domains of fixed domain length. These numerical modeling studies have also generally found less energy gain by the climate system with aggregation, because the increase in outgoing longwave radiation (from fewer high clouds and less water vapor greenhouse effect) outweighs any increase in absorbed solar radiation (from fewer high clouds), suggesting that aggregation might act as a negative feedback on climate change. However, self-aggregation has also been found to occur at temperatures much colder than current tropical values [*Abbot*, 2014; *Coppin and Bony*, 2015; *Wing and Cronin*, 2016; *Holloway and Woolnough*, 2016], drawing into question the supposed temperature-dependence of self-aggregation. While self-aggregation can apparently occur across a wide range of temperatures, the *degree* of aggregation may vary. Here, we explore two metrics of the degree of aggregation in the channel simulations across a 30 K range of temperatures from *Wing and Cronin* [2016] and the related dependence of circulation strength on temperature.

2.1 Degree of aggregation

Self-aggregation is associated with the tendency of the atmosphere to develop large regions of dry, subsiding air and the emergence of a large-scale overturning circulation. One metric that quantifies this is the "subsidence fraction", $f^{\downarrow}$, which has been used to assess ag-

gregation in GCM simulations with parameterized convection [*Coppin and Bony*, 2015; *Bony et al.*, 2016; *Becker et al.*, 2017]. We define the subsidence fraction as the fraction of the domain area with large-scale subsidence in the mid troposphere ($w < 0$ or $\omega > 0$ at 500 hPa); larger values of $f^{\downarrow}$ imply a greater degree of aggregation. Since we want to focus on large-scale subsidence analogous to what might be simulated in a GCM grid cell, we average the channel simulations over 96 $\times$ 96 km^2 blocks, and over a daily time period. The subsidence fraction shows substantial temporal variability, but increases from ∼0.5 to ∼0.7 as convection aggregates in each simulation (Figure 3a). Warmer simulations tend to have a smaller subsidence fraction than colder simulations, but the difference between the coldest and warmest simulations is less than 10% (<1 %°C^{-1}). Further, the simulations between T_S values of 280 K and 300 K have subsidence fractions that are nearly indistinguishable from each other (Figure 3a). These results are unchanged if the vertical velocity is instead averaged over 192 $\times$ 192 km^2 or 48 $\times$ 48 km^2 blocks, although the value of $f^{\downarrow}$ is smaller for a given simulation with a larger block size (Figure 3b). The results are also qualitatively similar if 5-day averages, instead of daily, and 192 $\times$ 192 km^2 blocks are used, although the sampling uncertainties for $f^{\downarrow}$ in the warm simulations are large. Note that aggregated square-domain simulations like those of *Wing and Emanuel* [2014] have a subsidence fraction of ∼0.85-0.9, and are thus more aggregated than the channel simulations by this metric (not shown). The GCM simulations of *Coppin and Bony* [2015] had subsidence fractions of $f^{\downarrow} \sim 0.65$ at $T_S < 294$ K, comparable to the values found here, and $f^{\downarrow} \sim 0.9$ at $T_S > 305$ K, larger than found here (their simulations at intermediate temperatures were disaggregated with $f^{\downarrow} \sim 0.55$, which does not occur in the channel simulations). In general, GCM studies have shown RCE simulations at the highest temperatures to be the most highly organized [*Coppin and Bony*, 2015; *Bony et al.*, 2016; *Pendergrass et al.*, 2016], which is the opposite of what we find here. One exception is *Narenpitak et al.* [2017], who performed cloud-resolving simulations of a large tropical channel with zonally-varying T_S, and found that changes in the shape of the distribution of column relative humidity with a uniform 4 K warming suggested a decrease in organization, broadly consistent with the results shown here.

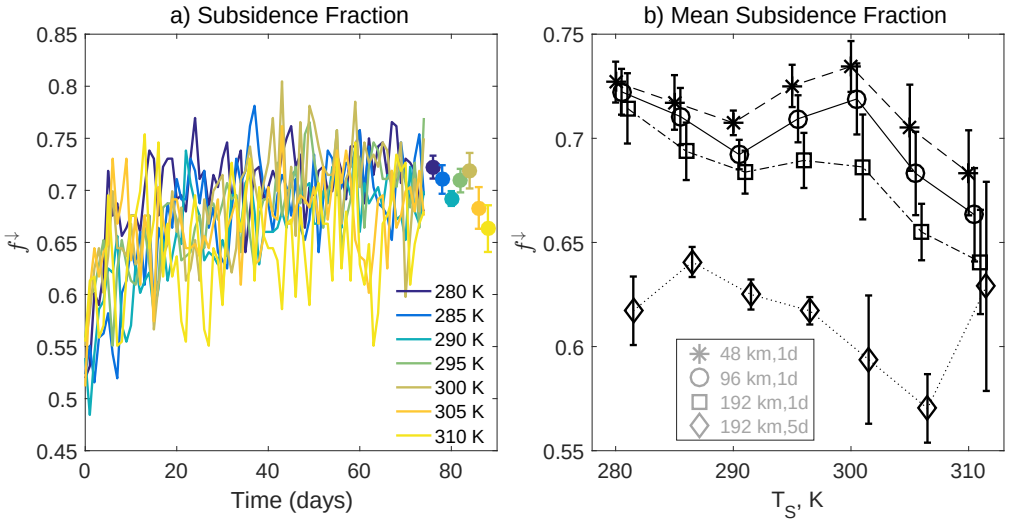

Figure 3. (a) Subsidence fraction $f^{\downarrow}$ plotted against time, in channel simulations at different T_S, using vertical velocity averaged over 96 $\times$ 96 km^2 blocks and 1 day. The average subsidence fraction over the last 25 days is plotted for each simulation in color-coded dots. (b) The average subsidence fraction over the last 25 days of each simulation plotted against surface temperature, for different block sizes and averaging periods. The error bars indicate bounds of the 5-95% confidence interval. The open circles are the same as the closed circles in (a). In (b), the points are offset slightly on the x-axis for visual clarity.

The subsidence fraction, $f^{\downarrow}$, emphasizes large-scale organization, but organization of convection takes place at multiple scales, any of which may vary with temperature. One alternative to the subsidence fraction is the organization index I_{org} of *Tompkins and Semie* [2017], which is based on the distribution of nearest neighbor distance between convective entities (see Appendix A for calculation methodology). This metric allows us to address the question of whether convective clouds are more or less clustered than a set of clouds with random locations [e.g., *Weger et al.*, 1992], where $\mathrm{I}_{org} > 0.5$ indicates aggregated convection. In the channel simulations for all surface temperatures, I_{org} increases quickly within the first few days of each simulation before reaching values between ∼0.75 and ∼0.90 (Figure 4). This metric indicates that the two coldest simulations (T_S of 280 K and 285 K) are less organized than the warmer simulations (in contrast to the results with the subsidence fraction metric), but there is not much variation in the organization index with further warming beyond $T_S = 295$ K. If convective pixels are defined as grid boxes in which the instantaneous cloud-top temperature is below 235 K (identifying cold, deep convective cloud tops) instead of using a vertical velocity threshold (see Appendix A), the values of I_{org} are smaller but the dependence on temperature is similar (Figure 4). Increasing clustering of convective entities with warming is broadly consistent with GCM simulations that show an abrupt transition to high degrees of organization at high temperatures [*Coppin and Bony*, 2015; *Bony et al.*, 2016; *Pendergrass et al.*, 2016], square domain convection-permitting simulations that only aggregate at $T_S > 300$ K [*Wing and Emanuel*, 2014], and theory [*Emanuel et al.*, 2014].

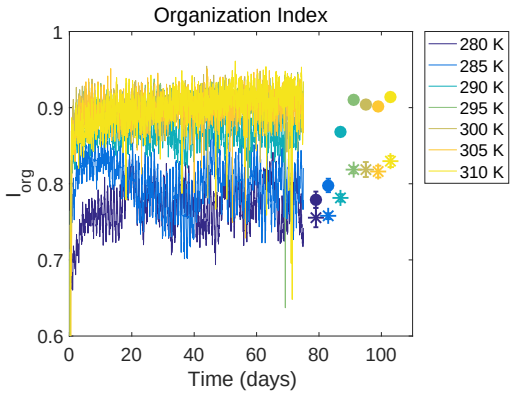

Figure 4. Time evolution of organization index I_{org}, where the average over days 50-75 is plotted for each simulation in color-coded dots (corresponding to the area under the colored curves in Figure A.1). The error bars indicate bounds of the 5-95% confidence interval. Stars (*) indicate I_{org} using the cloud-top temperature threshold to identify convective pixels; all other data use the vertical velocity threshold.

It is unclear which of the two metrics, subsidence fraction $f^{\downarrow}$ or organization index I_{org}, is more appropriate for defining the degree of aggregation in these simulations. Subsidence fraction is directly related to a transition that occurs as self-aggregation develops, towards small areas of strong ascent surrounded by large areas of weak subsidence. The organization index captures multiple scales of organization, including, to some extent, the large-scale moist and dry bands, but it is also heavily influenced by smaller-scale convective clustering within those bands. The organization index has the advantage of quantifying the extent of organization relative to a theoretically-based null distribution (a Poisson point process representing random convection), whereas we lack a null model for what the subsidence fraction should be in the absence of aggregation. Although the broad tendencies with warming of $f^{\downarrow}$ and I_{org} oppose one another, both metrics are relatively constant over large ranges of T_S. Further, a third metric of aggregation, the spatial variance of column relative humidity (used by *Wing and Cronin* [2016]), also has no clear temperature dependence (not shown). Thus, while the degree of aggregation does exhibit some temperature dependence, the nature of that dependence

is complicated and there is no clear trend towards an increase or decrease in aggregation with warming.

A further limitation of both metrics is that neither takes into account coherence of cloudy ascending regions in time, which is critical for how aggregation of convection translates into spatial variability of humidity. For example, strong instantaneous convective organization that propagated across the domain much more quickly than any location could dry out through subsidence in the absence of deep convection would lead to a nearly-homogeneous spatial distribution of relative humidity, rather than distinct moist and dry regions. *Craig and Mack* [2013] calculate the subsidence-drying time scale as the scale height of water vapor divided by the radiative-subsidence vertical velocity, and estimate this time scale as 2×10^5 seconds, or a little over two days. The radiative-subsidence velocity is given by

$$\omega_R = \frac{Q_R}{\frac{T}{\theta}\frac{d\theta}{dp}}, \tag{1}$$

and represents the subsidence that must occur to balance radiative cooling Q_R at steady state in non-convective regions of a non-rotating atmosphere. We calculate a vertically-averaged subsidence-drying time scale, $\overline{\tau_{\rm dry}}$, using an average pressure scale height of water vapor $\mathcal{P}_q = \left(\overline{d \log q/dp}\right)^{-1}$, and an average radiative-subsidence velocity $\overline{\omega_R}$ (zeroing ω_R in regions where it is negative):

$$\overline{\tau_{\rm dry}} = \frac{\mathcal{P}_q}{\overline{\omega_R}}, \tag{2}$$

where overlines indicate density-weighted vertical averages from 900 hPa to the top of the atmosphere. This vertically-averaged subsidence-drying time scale increases with warming from 3.5 d at 280 K to 6.6 d at 310 K, with near-constant rate of increase of about 0.1 d per K. The magnitude of $\overline{\tau_{\rm dry}}$ justifies our use of 5-day block averages in Figure 2 by showing that 5-day averages are long enough for pure radiative subsidence to appreciably dry the atmosphere. The dependence of $\overline{\tau_{\rm dry}}$ on surface temperature complicates thinking about the degree of aggregation, and suggests that aggregated convection could be less stationary at low temperatures and yet still influence relative humidity. Future development of metrics of convective organization might benefit from assessing the temporal coherence of convection or larger-scale vertical motion on time scales at least as large as $\overline{\tau_{\rm dry}}$. For example, the organization index of *Tompkins and Semie* [2017] could be adapted to include not only the convective entities at time t, but also the "ghost" entities from earlier time periods back to time $t - \overline{\tau_{\rm dry}}$.

2.2 Circulation changes

Changes in the large-scale circulation are linked to the subsidence fraction, $f^{\downarrow}$. Following *Bony et al.* [2013], we define $I = \overline{\omega^{\downarrow}} - \overline{\omega^{\uparrow}}$ as the intensity of the large-scale circulation, where $\overline{\omega^{\downarrow}}$ is the mean 500-hPa pressure velocity in large-scale (192×192 km^2) blocks with descent, and $\overline{\omega^{\uparrow}}$ is the mean 500-hPa pressure velocity in large-scale blocks with ascent. We find that I decreases steeply with warming, by $\sim$6 %°C^{-1}, as distributions of both large-scale ascent and subsidence collapse toward $\omega = 0$ with warming; the large-scale circulation therefore weakens as the surface is warmed (Figure 5a; note that the brown curve in Figure 5a is the same as the red-dashed curve in Figure 2).

The subsidence fraction at the block size of 192×192 km^2 and for 5-day averages is $f^{\downarrow}$ $\sim$ 0.6, and shows a slight but non-monotonic decrease as the surface is warmed (Figure 3b). The relatively constant subsidence fraction at this block size implies that I, $-\overline{\omega^{\uparrow}}$, and $\overline{\omega^{\downarrow}}$ must all scale together with a warming surface, since continuity implies:

$$-\overline{\omega^{\uparrow}} = \frac{f^{\downarrow}}{1 - f^{\downarrow}}\overline{\omega^{\downarrow}}, \tag{3}$$

$$I = \frac{1}{1 - f^{\downarrow}}\overline{\omega^{\downarrow}}. \tag{4}$$

Even allowing for a change in $f^{\downarrow}$ with warming – e.g., the small decrease across the overall 30 K range of T_S with 1-day averages (Figure 3b) – the decrease in I is far too strong to be explained by the changes in subsidence fraction. Figure 5b indeed shows $-\overline{\omega^{\uparrow}} \approx 1.5\overline{\omega^{\downarrow}}$ and $I \approx 2.5\overline{\omega^{\downarrow}}$ across the range of surface temperatures; thus, given a constraint on one of subsidence, ascent, or overall circulation intensity, it follows that the scaling of the whole circulation with warming could be diagnosed.

One such constraint is the thermodynamic throttle on large-scale subsidence in areas devoid of deep convection [e.g., *Knutson and Manabe*, 1995; *Held and Soden*, 2006], which might connect $\overline{\omega^{\downarrow}}$ to the radiative-subsidence vertical velocity ω_R (Eqn. (1)). Figure 5b shows that ω_R, evaluated at 500 hPa, is about 50% larger than the mean downward velocity in subsidence regions, and declines with warming at nearly the same rate as I, $-\overline{\omega^{\uparrow}}$, and $\overline{\omega^{\downarrow}}$. The decline in ω_R occurs primarily due to increasing stability $|\frac{d\theta}{dp}|$ with surface warming. Thermodynamics of clear-sky radiative cooling thus constrain the response of the whole circulation to warming in our simulations. This result is not a foregone conclusion even with the constraint of weakly-varying subsidence fraction; for example, the distribution of convective heating in regions of large-scale subsidence could change with warming in such a way as to make the relationship between $\overline{\omega^{\downarrow}}$ and ω_R depend on temperature. Such changes, however, do not seem to be of first-order importance in our simulations. One exception is the slight increase in circulation intensity from 305 K to 310 K, despite the thermodynamic-driven weakening, which is linked to an increase in the subsidence fraction for that block size (Figure 3b). The weak dependence of subsidence fraction on surface temperature is both key to this scaling argument and also notable in its own right, since self-aggregation of convection can result in a wide range of large-scale subsidence fractions [e.g., *Coppin and Bony*, 2015; *Reed et al.*, 2015; *Wing*, 2014].

Similar results have been found in GCMs for the weakening of the Walker circulation with global warming [*Vecchi and Soden*, 2007; *Merlis and Schneider*, 2011], but their findings have often been framed in terms of relative changes in precipitation and boundary layer specific humidity, with the goal of understanding the mean vertical velocity and convective mass fluxes in ascending regions. These two perspectives of radiative subsidence in dry regions and water balance in moist regions are complementary for circulations with fixed geographic extent, since they both rely on energy balance. Our arguments about increasing static stability leading to decreasing circulation strength likely apply better to the Walker circulation than to the Hadley circulation, because poleward expansion of the Hadley circulation with warming may lead to an increase in the subsidence fraction. The Hadley circulation is also constrained by rotation and extratropical influences in ways that the Walker circulation is not.

3 Clouds

A striking consequence of self-aggregation is the spatial reorganization of the cloud field and the reduction in high cloud cover [e.g., *Tobin et al.*, 2013; *Wing and Cronin*, 2016]. *Bony et al.* [2016] used RCE simulations in several GCMs to assess changes in clouds with warming; we examine similar changes in the channel simulations. In the channel simulation at T_S= 300 K, there is a lower-tropospheric peak in liquid cloud water concentration of ∼23 mg m^{-3} near 870 hPa, a mid-level minimum in cloud water near 600 hPa, and an upper-level peak in ice cloud water of ∼4.5 mg m^{-3} near 375 hPa (Figure 6a). This overall shape in the cloud water profile compares well with tropical observations from CloudSat [*Su et al.*, 2011, their Figure 2, replotted in green on Figure 6a], with a good quantitative match of cloud water concentration in the lower troposphere. This agreement in the lower troposphere is surprising given the relatively coarse horizontal resolution of 3 km used here, and it may not be meaningful because the channel simulations lack realistic trade-cumulus and stratocumulus cloud regimes in which much of the lower-tropospheric tropical cloud water is found. Despite the lack of realistic inversion environments in the channel simulations, we find it notable that the channel simulations have both greater lower-tropospheric stability (by $\sim 0.5 - 1$ K over the 100-hPa layer centered on 850 hPa near the level of peak cloud water) and more lower-

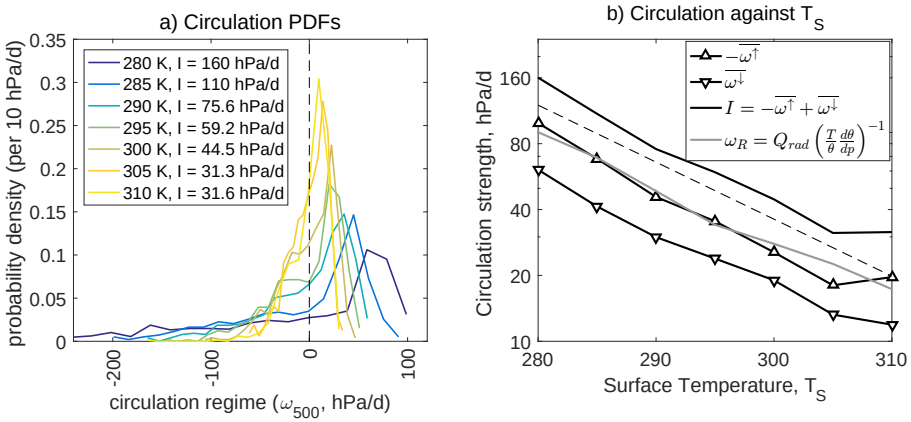

376 **Figure 5.** Large-scale circulation and its dependence on surface temperature. a) Dynamical regime his-
377 togram across a range of T_S, calculated from 192 x 192 km^2 block averages of 500-hPa vertical velocity over
378 5-day windows from days 25-75 of each simulation. b) Mean pressure velocity in blocks with ascent $-\overline{\omega^{\uparrow}}$ and
379 subsidence $\overline{\omega^{\downarrow}}$, as well as circulation intensity I, and radiative-subsidence pressure velocity ω_R (Eqn. 1). The
380 thin dashed line in b) is drawn for reference, and decreases by $6\%^{\circ}\mathrm{C}^{-1}$; note the logarithmic vertical axis in
381 b).

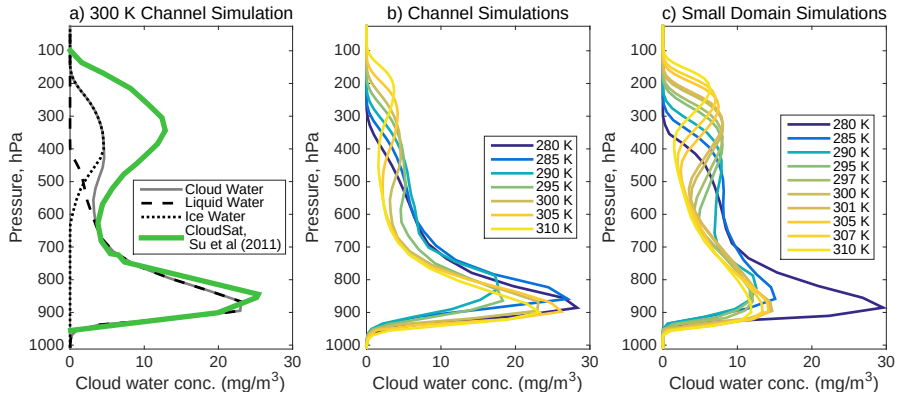

411 **Figure 6.** Domain average profiles of cloud water concentration (mg m^{-3}) over the final 25 days of sim-
412 ulation in a) the 300 K channel simulation (green line indicates cloud water profile from observations by
413 CloudSat), b) all channel simulations, and c) the small-domain simulations. The liquid cloud water concentra-
414 tion (dashed line) and ice cloud water concentration (dotted line) is also shown in a).

399 tropospheric cloud water (by a factor of 1.5-2) relative to the small-domain simulations. Our
400 channel simulations may thus be getting the right answer for the lower-tropospheric cloud
401 peak for partially meaningful reasons, since the linkage between lower-tropospheric stability
402 and cloudiness also exists in the real world [e.g., *Klein and Hartmann*, 1993]. The largest
403 deficiency in the 300 K channel simulation relative to CloudSat observations is too little cloud
404 ice; the peak in ice cloud water concentration in observations is about three times larger than
405 in our simulations . This lack of anvil cloud ice likely has implications for the magnitude of
406 the cloud radiative forcing in our simulations, and may occur due to rapid sedimentation of
407 cloud ice. Notably, the cloud water concentration in the channel simulation compares better
408 to observations than does the simulated cloud water in GCMs [*Su et al.*, 2011, their Figure 2]
409 – indicating that there is value in using the channel simulations to study cloud changes and
410 feedbacks.

3.1 Cloud changes

We diagnose cloud fraction as the fraction of the total domain covered by cloud at a given level, where "cloud" is defined according to a threshold of 0.01 g kg^{-1} of total cloud (liquid water + ice) condensate. High clouds shift upwards and decrease in amount with warming (Figure 7a), in agreement with the GCM simulations of *Bony et al.* [2016] but in opposition to the CRM simulations of *Singh and O'Gorman* [2015] and global explicit convection simulations of *Satoh et al.* [2017]. Anvil temperature also increases more slowly than surface temperature by a factor of 3-4, from ∼215-225 K (Figure 7b), which is more consistent with the "proportionately higher anvil temperature" hypothesis of *Zelinka and Hartmann* [2010] than with the more stringent "fixed anvil temperature" hypothesis of *Hartmann and Larson* [2002]. The average upper-level cloud water concentration increases with warming up to T_S = 290 K, but then decreases with further warming (Figure 6b). Mid-level clouds decrease sharply with warming (Figures 6b,7a), more notably than in the GCM simulations of *Bony et al.* [2016], but those GCMs are known to lack mid-level clouds in the first place [e.g., *Zhang et al.*, 2005; *Cesana and Chepfer*, 2012]. Low cloud amount decreases overall with warming, but the decrease is concentrated at the coldest surface temperatures we simulate, and is not monotonic above 290 K (Figures 6b,7a). The height of the low cloud maximum also decreases overall with warming, but non-monotonically.

Similar cloud changes also occur in small-domain simulations without any self-aggregation or large-scale circulations (Figures 7c,d), suggesting they are a basic response to warming and not a result of self-aggregation or changes in aggregation with warming. The main impact of self-aggregation appears to be a reduction in high cloud amount; at a given T_S, the high cloud fraction and cloud water concentration is larger in the small-domain simulations (Figures 6c, 7c) than in the channel simulations (Figures 6b, 7a). This response of decreasing high cloud fraction with aggregation is similar to that inferred from observations [*Stein et al.*, 2017]. Changes in average cloud water concentration at high levels are similar in the two sets of simulations, although the cloud water does not start to decrease with warming until T_S = 300 K in the small-domain simulation (Figure 6b,c). With the exception of the simulation at T_S = 280 K, the small-domain simulations have less low cloud amount than their channel simulation counterparts (Figures 6, 7). This opposing response of low and high clouds to self-aggregation was also noted by *Wing and Cronin* [2016], who found that the differences roughly cancelled each other out such that the amount of reflected shortwave radiation was largely unchanged by self-aggregation.

The anvil cloud fraction, defined as the local maximum of time-mean cloud fraction in the upper troposphere over the final 25 days of simulation, decreases by ∼0.002 $°C^{-1}$, or a ∼2 $\%°C^{-1}$ relative decrease, in the channel simulations (Figure 8). The anvil cloud fraction decreases at a greater relative rate in the small-domain simulations (∼3 $\%°C^{-1}$), but if the coldest simulation (T_S = 280 K) is ignored as an outlier with substantially more clouds than the other simulations, the anvil cloud fraction also decreases at a rate of ∼2 $\%°C^{-1}$. We reiterate our earlier point that the existence of self-aggregated convection and large-scale circulations in the channel simulations act primarily to reduce the absolute amount of high cloud cover; self-aggregation and changes in self-aggregation with warming do not significantly change the response of clouds to warming. One subtle difference, though, between the changes in anvil cloud fraction in the two sets of simulations, is that the cloud fraction decreases more quickly with warming in the small-domain simulations over the 300-310 K temperature range. We speculate that this is because the anvil cloud fraction in the channel simulations has reached such small absolute values that it is difficult for it to decrease much further – perhaps reflecting a constraint on the convective area that sets a lower bound on anvil cloud amount, as suggested by *Bony et al.* [2016].

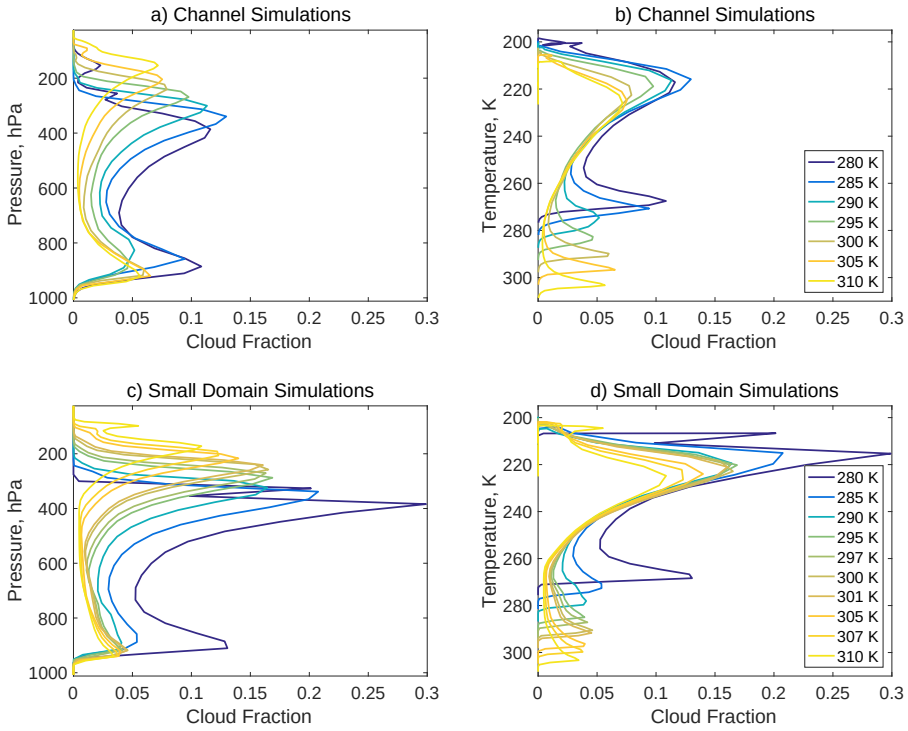

464 **Figure 7.** Domain average vertical profiles of cloud fraction from (a,b) channel simulations and (c,d) small-
465 domain simulations, averaged across the final 25 days of the simulation, with profiles plotted against (a,c)
466 pressure and (b,d) temperature.

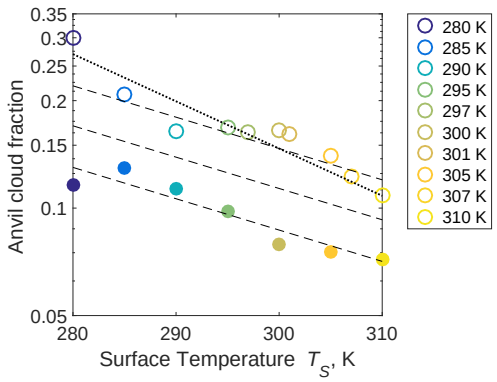

467 **Figure 8.** Anvil cloud fraction (averaged over final 25 days of simulation) versus sea-surface temperature
468 from small-domain (open circles) and channel simulations (filled circles). The thin dashed lines are drawn for
469 reference and decrease by 2 $\%^{\circ}\mathrm{C}^{-1}$; the thin dotted line decreases by 3 $\%^{\circ}\mathrm{C}^{-1}$. Note the logarithmic vertical
470 axis.

3.2 High cloud changes

Bony et al. [2016] introduced a "stability-iris" hypothesis to explain the reduction in anvil cloud fraction with warming. They argued that as the climate warms, anvil clouds rise and remain at nearly the same temperature but find themselves in a more stable atmosphere. Further, the anvil cloud amount is suggested to relate to the horizontal mass divergence in cloudy, convective regions, which must match the horizontal mass convergence in clear-sky regions by mass conservation. Because stability at cloud level increases with warming, less horizontal divergence from cloudy regions is required to balance the vertical gradient in clear-sky radiative cooling, leading to reduced anvil cloud amount.

We find that the relationships between anvil cloud fraction, radiatively-driven divergence, static stability, and surface temperature in our simulations are consistent with those of *Bony et al.* [2016]. This consistency is not a completely independent verification of *Bony et al.* [2016], since *Bony et al.* [2016], in addition to using GCM simulations, also examined the response of anvil cloud fraction to warming in the channel simulations of *Wing and Cronin* [2016], which are similar to the simulations examined here, except for the use of a different radiation scheme. Following *Bony et al.* [2016], we define radiatively-driven divergence as $D = d\omega_R/dp$ where the radiative-subsidence velocity is given by Eqn. (1). Note that D is a divergence of the vertical (pressure) velocity in clear-sky regions, which by mass continuity implies convergence of the horizontal flow in clear areas, and must in turn be balanced by a divergence of the horizontal flow out of cloudy regions. All variables are computed from domain-average profiles, averaged over the final 25 days of simulation and are shown in Figure 9. The anvil cloud fraction (the local maximum of cloud fraction in the upper troposphere) increases roughly linearly with the maximum in upper-tropospheric radiatively-driven divergence, except when going from 280 K to 285 K (Figure 9a), indicating that the anvil cloud amount is related to the amount of divergence. In addition, the level of the maximum radiatively-driven divergence matches very well with the level of maximum high cloud fraction (not shown). The stability (at the level of the maximum divergence) increases with surface temperature, approximately following the stability at a constant temperature of 220 K (Figure 9b). This indicates that, with warming, anvil clouds indeed occur in a more stable environment. The radiatively-driven divergence decreases with the stability, consistent with the idea that, in a warmer atmosphere, less divergence of ω is needed to balance the vertical gradient in radiative cooling (Figure 9c). All of these relationships are found both in the channel simulations (with self-aggregation) and in the small-domain simulations (*without* self-aggregation), providing further evidence of a fundamental response of clouds to warming, independent of self-aggregation. One difference between the channel and small-domain simulations is that there is a cluster of small-domain simulations (from 295-301 K) for which the anvil cloud fraction does not really change with warming (Figure 8). This cluster, however, is consistent with the divergence and stability arguments, as the maximum radiatively-driven divergence also does not vary over that temperature range in the small-domain simulations (Figure 9a).

Although the high cloud changes with warming in our simulations are consistent with the "stability-iris" arguments of *Bony et al.* [2016], they may also be consistent with alternative interpretations. *Seeley et al.* [2017] have very recently suggested that a combination of cloud lifetime and gross detrainment from clouds, rather than radiatively-driven divergence (which is related to net detrainment from clouds), controls the shape of the anvil cloud peak in the upper troposphere, and how it scales with warming or other changes to the environment. In the upper troposphere, where mixing is very inefficient at getting rid of clouds, microphysical removal processes that convert cloud ice into snow, or lead to sedimentation of cloud ice, may become important in setting the location and magnitude of the anvil cloud fraction peak. If these processes depend on temperature or pressure, they may also influence how the anvil cloud fraction depends on surface warming. Preliminary investigation suggests that the scaling of anvil cloud fraction in our simulations with both temperature and domain size may be predicted just as well by the lifetime-based argument of *Seeley et al.* [2017] as by the radiatively-driven subsidence argument of *Bony et al.* [2016]. The scaling of *Seeley et al.*

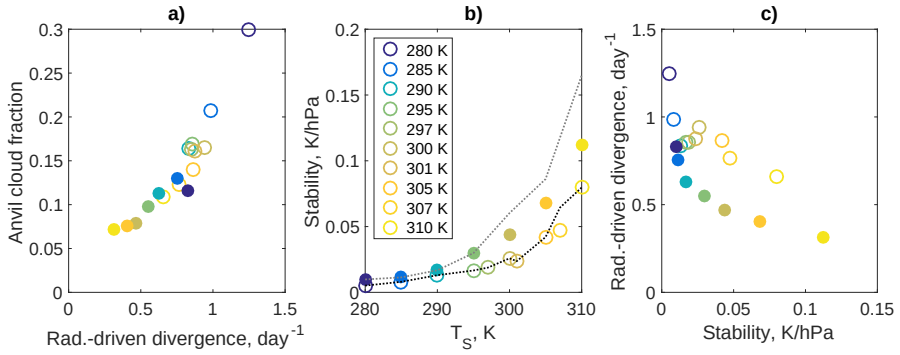

Figure 9. Relationship between a) anvil cloud fraction and radiatively-driven divergence, b) static stability at the level of maximum divergence and sea-surface temperature (and along the 220K isotherm, dotted line), and c) radiatively-driven divergence and static stability at the level of maximum divergence, for both small-domain (open circles) and channel simulations (filled circles). Values are averages over the final 25 days of each simulation.

[2017], however, is not as straightforward to apply because it is sensitive to assumptions about detrainment and cloud microphysical processes, which are difficult to diagnose from SAM after a simulation has been conducted. Furthermore, even though the two theories can give very different results in some cases, they might make similar predictions in our case. Convergent predictions by the two theories should be expected if 1) net detrainment dominates gross detrainment in the upper troposphere, and 2) the removal time scale of cloud ice is constant with height and surface temperature. Both of these conditions may be satisfied in our simulations, because the cloud mass flux decays rapidly with height near the anvil cloud peak, and the lifetime of high thin clouds with the bulk microphysics scheme we have used is strongly regulated by ice sedimentation, which is a weakly nonlinear function of cloud ice content only (i.e., it does not depend explicitly on either pressure or temperature).

3.3 Mid-level cloud changes

We have focused thus far on changes in high clouds because they account for a large portion of total cloud cover in our simulations, and also because they have been the subject of prior study. The sharp decline in mid-level cloud fraction with warming, however, is at least as notable a feature of Figure 7 as the upward shift and reduction in high cloud amount. Moreover, mid-level cloud fraction from the mid-level minimum up to higher altitudes nearly collapses onto a single curve when plotted as a function of temperature, for all $T_S > 280$K (Figure 7b).

Why should mid-level cloud fraction decrease so precipitously with warming? And what sets the shape of mid-level cloud fraction in temperature space? Mid-level clouds in our simulations are almost entirely convective – there is little mid-level stratiform cloud both because the mid-troposphere is dry, and because few clouds reach their level of neutral buoyancy and experience strong detrainment in the mid-troposphere. The convective nature of mid-level clouds implies that they transport heat, and this can in turn be used as a basis for a scaling argument for both their declining amount with warming, and their common shape when plotted with temperature as a vertical coordinate. We find this argument intriguing enough to present as a hypothesis, but admit at the outset that it is highly speculative.

Working with temperature T as our vertical coordinate, we begin by assume that the approximate convective enthalpy flux $F_c = \sigma_c w_c [L_v \rho_v^* (1 - \mathrm{RH}) + \delta s]$ by mid-level cumulus balances radiative cooling Q of the overlying troposphere. Here, σ_c is the cloud fraction, w_c

is the in-cloud vertical velocity, and $L_v\rho_v^*(1-\mathrm{RH})$ is the latent heat excess per unit volume carried upwards by clouds relative to the subsiding unsaturated environment, where RH is the relative humidity, and $\rho_v^* = e^*/(R_vT)$ is the saturation vapor density, which is a function of temperature only. The last term in the convective enthalpy flux includes δs, the dry static energy excess per unit volume carried upward by clouds; this term is most important in the upper troposphere, where latent heat transport by convection becomes small. Aside from our inclusion of this δs term, which prevents the cloud fraction from blowing up when the vapor density becomes small, we have made the approximation of low-buoyancy clouds, which have a small temperature excess compared to the unsaturated environment [*Singh and O'Gorman*, 2013]. Note also that this is only an approximation of the full convective enthalpy flux because it ignores covariance between moist enthalpy and vertical velocity within categories of of both cloudy air and unsaturated environment.

The radiative cooling Q is equal to an integral of the radiative cooling rate $J(T)$, expressed as a function of temperature (with units W m^{-2} K^{-1}) and integrated upward from temperature level T to the tropopause temperature T_T. Writing this out explicitly and rearranging to solve for the cloud fraction gives:

$$\sigma_c(T) = \frac{\int_{T_T}^{T} J(T')dT'}{w_c[L_v\rho_v^*(1-\mathrm{RH}) + \delta s]} \tag{5}$$

All of these terms roughly collapse across different values of T_S when taken to be functions of temperature as a vertical coordinate (Figure 10). This collapse is only seen if we restrict our attention to the mid-level cloud fraction minimum and above (i.e., to higher altitudes), because the temperature at the top of the boundary layer, with its local cloud maximum, increases as the surface warms. A reasonably sound argument from basic principles of radiative transfer can be provided for why $J(T)$ is a nearly universal function of temperature [*Ingram*, 2010; *Jeevanjee and Romps*, 2016], but overall this scaling argument is primarily diagnostic. Particularly glaring issues are the lack of explanation for what sets w_c, and the arbitrary use of updraft minus downdraft core dry static energy difference as our scale for δs. Note that RH has been argued to be a function of temperature only by Romps, 2014 – but the particular function depends on the scale height of mass exchange between convection and the environment, which is also uncertain. Furthermore, even though Figure 10 appears to show that the collapse of RH onto a single function is the least clean of all pieces of this argument, order-1 differences in the radiative cooling integral across values of T_S also appear in the upper troposphere – they are just more difficult to see because the general shape of each curve over the whole troposphere is similar. Despite these issues, the scaling argument provides a simple explanation for why mid-level cloud fraction decreases with warming: the product of cloud updraft speed and cloud vapor density excess increases with temperature much faster than does the radiative cooling of the overlying troposphere [this argument is similar to but more quantitative than the one made by *Held and Soden*, 2006]. This scaling also suggests that relative humidity may influence mid-level cloud fraction indirectly through its constraints on the convective latent heat flux: other things equal, an atmosphere with higher relative humidity requires more convective cloud area in order to transport the same amount of heat upwards.

4 Climate Sensitivity

The rate of change of net top-of-atmosphere energy gain R with increasing surface temperature gives us an estimate of the net climate feedback, $\lambda = dR/dT$. These "Cess-type" net feedbacks [e.g., *Cess and Potter*, 1988] in our simulations can then be directly compared to feedbacks calculated using the local framework in a general circulation model [e.g., *Feldl and Roe*, 2013a]. Climate sensitivity to a doubling of CO_2 could be crudely estimated as $\Delta T_{2\times} = -F_{2\times}/\lambda$, where $F_{2\times} = 3.7$ W m^{-2} approximates the global-mean radiative forcing from doubling CO_2 [*Ramaswamy et al.*, 2001]. We will focus on discussion of feedbacks, however, rather than converting to climate sensitivity, because $F_{2\times}$ would likely increase with sea-surface temperature as the thermal contrast across the troposphere widens – this is the

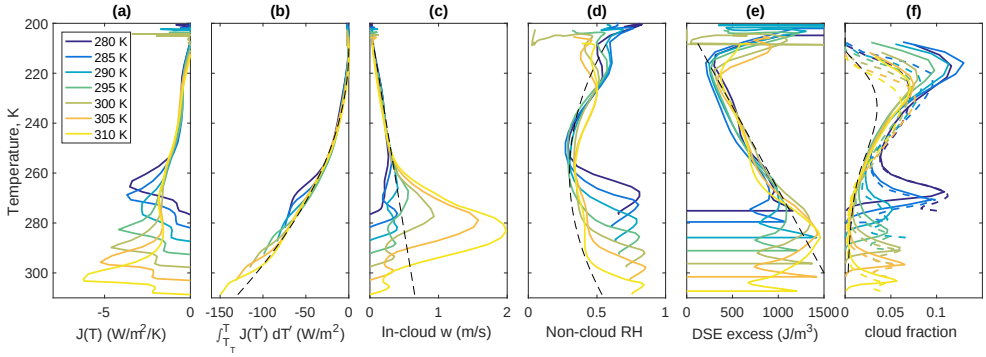

Figure 10. Terms in diagnostic scaling for mid-level cloud fraction (equation 5), all plotted as profiles against domain-mean temperature: a) radiative cooling rate in temperature coordinates, b) integrated radiative cooling of overlying troposphere, c) in-cloud vertical velocity, d) relative humidity of non-cloudy air, e) dry static energy excess of updraft core minus downdraft core, f) cloud fraction. Black dashed lines in b)-e) indicate approximate fits for each term as a function of temperature, and the black dashed line in f) indicates how these functions together with equation 5 approximate the cloud fraction profile. Colored dashed lines in f) indicate how the SST-dependent profiles in b)-e) combine with equation 5 to approximate the cloud fraction profile.

same reason that CO_2 radiative forcing is larger in the tropics than in polar regions in global models [e.g., *Huang et al.*, 2016].

Based on linear regression of top-of-atmosphere fluxes across the whole range of surface temperatures for simulation days 50-75, the average net climate feedback in the channel simulations is $\lambda = -1.91 \pm 0.1$ W m^{-2} K^{-1} (Figure 11a; in this section we use $\pm$ to indicate 5-95% confidence intervals about the mean). The temperature-averaged net feedback in the small-domain square simulations is $\lambda = -1.23 \pm 0.16$ W m^{-2} K^{-1} – about 0.7 W m^{-2} K^{-1} less negative than the channel simulations (Figure 11a). Analyzing feedbacks over 5-K increments in surface temperature, λ is negative across all temperatures in the channel simulations, but dependence of the net feedback on sea-surface temperature is non-monotonic, with the most negative feedback (-2.5 W m^{-2} K^{-1}) from 290 to 295 K, and the least negative feedback (-1.5 W m^{-2} K^{-1}) between 285 to 290 K and 300 to 305 K (black diamonds in Figure 11c). The small-domain simulations (gray diamonds in Figure 11c) show a less negative feedback over most but not all temperature ranges, and an unstable net feedback over the temperature range of 280-285 K which is associated with a strong decrease in cloudiness and increase in total cloud radiative forcing (CRF) with warming over this range (Figures 7 and 11b). Total cloud radiative forcing tends to increase slightly with surface warming for both channel and small-domain simulations, but this trend is nonmonotonic, and the slope of CRF with temperature is not significantly different from zero for either geometry at the 95% confidence level (Figure 11b).

A major limitation of Cess-type feedback analysis is that cloud radiative feedbacks can only be crudely estimated from changes in cloud radiative forcing (e.g., Figure 11b). Radiative kernels use offline calculations with a radiative transfer model to calculate partial derivatives of top-of-atmosphere fluxes with respect to temperature and specific humidity, and can be used to correct changes in cloud radiative forcing with warming; such correction provides our best current estimates of cloud feedbacks [e.g., *Soden et al.*, 2008]. Kernel-based corrections generally also require changes in surface albedo and radiative forcing, but neither of these terms is relevant here since surface albedo is constant, and insolation and greenhouse gases are held fixed across surface temperatures. To understand how the cloud radiative feedbacks in our simulations compare to global models, we use offline calculations with the RRTMG

model [*Iacono et al.*, 2008] to generate approximate humidity-sorted radiative kernels and thus correct the changes in CRF that occur with warming in our simulations. These approximate radiative kernels also allow us to decompose the non-cloud feedbacks into Planck, lapse rate, and water vapor components.

The methodology for calculation of these kernels is presented in Appendix B.1, and the overall results for kernel-corrected cloud feedback are shown in Figure 11c; open circles indicate the combined water vapor and temperature feedbacks, λ_{T+q} (or the total non-cloud feedback), and filled circles indicate the cloud feedback λ_{cloud}, for each 5K increment of warming. The small black and gray dots in Figure 11c are residuals of the kernel method; their proximity to zero shows that the approximate kernel method works adequately. Kernel-correction of the cloud feedbacks causes them to be slightly more positive – by about 0.15 W m^{-2} K^{-1} for the channel simulations and a larger 0.33 W m^{-2} K^{-1} for the small-domain simulations when the corrections are averaged across all temperatures. The larger correction in the small-domain simulations occurs because they have a larger cloud fraction, and thus a larger difference between all-sky and clear-sky kernels. Note also that the magnitude of correction in the small-domain simulations is smaller than the correction in GCMs of 0.48-0.68 W m^{-2} K^{-1} found by *Soden et al.* [2008], but CRF correction in GCMs includes additional terms associated with surface albedo changes. If the kernel corrections could be considered error-free, then adding them to the average CRF change with warming from Figure 11b would give $\lambda_{\mathrm{cloud}} = 0.25 \pm 0.12$ W m^{-2} K^{-1} for the channel simulations and $\lambda_{\mathrm{cloud}} = 0.52 \pm 0.23$ W m^{-2} K^{-1} for the small-domain simulations; these are both significantly different from zero with $>$95% confidence, but do not differ significantly from each other at the 95% confidence level. It is unclear how sampling errors in temperature and humidity should be propagated through the kernel correction of CRF, so we hesitate to assign a more specific confidence level to how different the cloud feedbacks are in the two domain geometries. This caveat noted, we conclude that the total cloud feedback is weakly but significantly positive in both geometries when averaged across the whole temperature range.

Overall, the results shown here are consistent with the findings of *Mauritsen and Stevens* [2015] that convective aggregation has a modest but significant effect on reducing climate sensitivity. Our best estimate across all temperatures is that total feedbacks are more negative by 0.68 W m^{-2} K^{-1} in the channel simulations than in the small-domain square simulations, with contributions from both a more negative non-cloud feedback (by 0.41 W m^{-2} K^{-1}) and a less positive cloud feedback (by 0.27 W m^{-2} K^{-1}). Kernel-corrected cloud feedbacks in both geometries are significantly positive when averaged over all temperatures, and the kernel correction makes them more different from both zero and from each other. Even after including the kernel correction, however, the cloud feedbacks averaged across all temperatures do not significantly differ between geometries. Furthermore, variability in the net feedbacks and cloud feedbacks across temperatures is large in both geometries and prevents us from making simple conclusions about the climate feedbacks over narrower temperature ranges. This variability arises due to both temporal variability in top-of-atmosphere fluxes for a single simulation, and subtle variations in the degree of aggregation and cloudiness across simulations. Use of radiative kernels in RCE thus allows for better characterization of radiative feedbacks and a clearer relation of them to feedbacks in GCMs, but is also limited by our poor understanding of the low-frequency variability in cloud cover, relative humidity, and the degree of aggregation in RCE, and methodological uncertainty in how to best propagate sampling errors in feedback through radiative kernels.

5 Conclusions

This paper has sought to analyze the clouds, circulation, and climate sensitivity in channel simulations of RCE. Below, we summarize our main findings, and refer the reader back to the sections where they were presented:

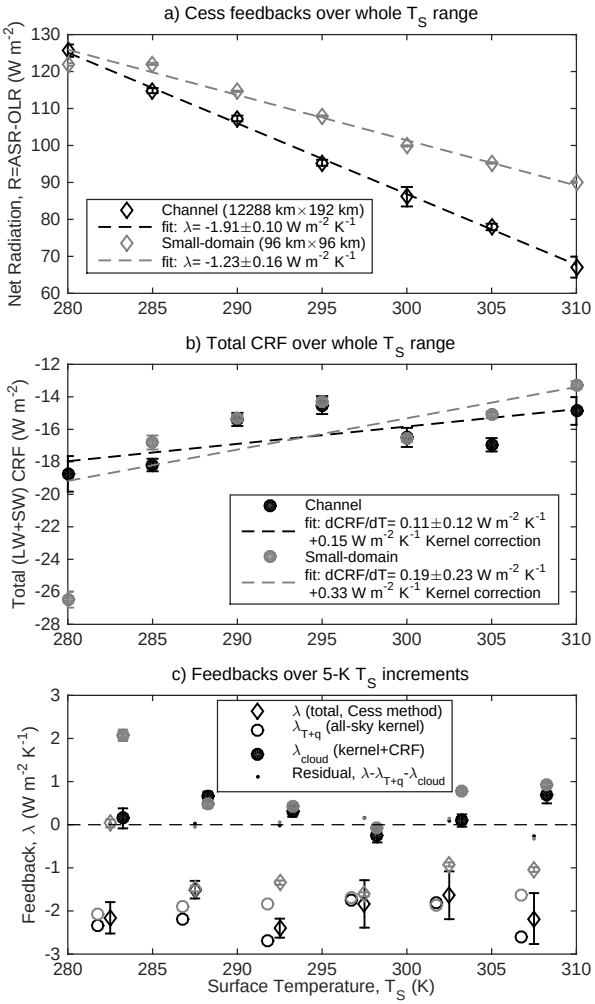

Figure 11. a) Top-of-atmosphere net radiation R against SST for channel simulations (black diamonds), small-domain square simulations (gray diamonds), and linear regressions to each (dashed black and gray lines, respectively). b) Total cloud radiative forcing (CRF) against SST for channel simulations (filled black circles), small-domain square simulations (filled gray circles), and linear regressions to each. The legend in b) also shows for each geometry the average kernel-based correction to the slope $d\mathrm{CRF}/dT$, that is used to calculate kernel-corrected cloud feedbacks (see Appendix B.1). c) Net feedback (open diamonds), kernel-based all-sky temperature plus water vapor feedbacks (open circles), kernel-corrected cloud feedbacks (filled circles), and residual from the kernel method (small dots), for each 5K SST interval, with channel simulations in black and small-domain square simulations in gray (see Appendix B.1 for radiative kernel methodology). The kernel-based feedbacks are slightly offset from the midpoint of each 5K SST interval for visual clarity. Linear regressions in a) and b) are weighted by the inverse variance of the net daily flux over days 50-75 of each simulation, and confidence intervals indicated with error bars are 5-95%, based on the standard error of daily-mean fluxes (or difference of daily-mean fluxes over 5K SST intervals in c), with number of degrees of freedom reduced to account for temporal autocorrelation.

- Self-aggregation in channel RCE simulations generates a realistic distribution of large-scale vertical motion . (Section 1.2)
- The changes in the degree of aggregation with warming are complicated and depend on the metric chosen; there is no obvious trend with warming towards more or less aggregation. (Section 2.1)
- The intensity of the overturning circulation weakens with warming and scales with the clear-sky radiative subsidence, which decreases primarily because of increasing stability. The circulation strength is only weakly dependent on subsidence fraction. (Section 2.2)
-
- High clouds shift upward and reduce in extent with warming, at approximately the same relative rate of -2% K^{-1} in simulations both with and without aggregation, though anvil cloud fraction is reduced in simulations with aggregation. The high cloud changes are consistent with the stability iris hypothesis of *Bony et al.* [2016]. (Sections 3.1, 3.2)
- Mid level cloud fraction decreases sharply with warming. We introduce a diagnostic scaling argument that interprets this decrease as due to more rapid increases with warming of the product of cloud updraft speed and vapor density, as compared to radiative cooling of the overlying troposphere. (Section 3.3)
-
- We calculate a net climate feedback of -1.9 $\pm$ 0.1 W m^{-2} K^{-1} in the channel simulations, and we find that the climate sensitivity is lower with aggregation (channel simulations) than without (small simulations) . (Sections 4, B.2)
- We introduce an approximate humidity-sorted radiative kernel method for RCE, discuss features of this kernel relative to GCM-based kernels, and use it to correct cloud feedbacks and decompose non-cloud feedbacks. The kernel-corrected cloud feedback is found to be positive, and on the lower end of GCM estimates. (Appendix B)

To repeat the point made at the end of the introduction, we believe that the combination of realistic large-scale dynamical regimes and resolved deep convection in the long-channel RCE model configuration provides a rich tool for exploring how clouds, circulation, and top-of-atmosphere energy balance depend on climate warming.

This work has numerous limitations. Although our choice of horizontal resolution, at 3 km, is sufficient to permit deep convection, it is coarse enough that the subgrid-scale parameterization of turbulence is important for mixing between clouds and the environment, which influences free-tropospheric relative humidity [*Romps*, 2014] as well as the lifetime and properties of shallow clouds. From a standpoint of tropical climate feedbacks, our simulations also lack a key cloud regime – stratocumulus – which may be particularly sensitive to warming and may contribute to a strong positive shortwave cloud feedback in the real world. Including a wavenumber-1 sinusoidal variation of sea-surface temperature along the channel, as in *Wofsy and Kuang* [2012], might be a way to obtain stratocumulus in the regions of coolest SST, but introduces an additional dimension to parameter space (the SST contrast between warm and cold regions). As discussed above, our high clouds have too little ice water content as compared to observations – which may reduce the potential for a positive shortwave feedback as their coverage diminishes with warming. It is possible that uncertain parameters in the microphysics scheme, such as cloud ice autoconversion threshold and sedimentation velocity, could be tuned to give a better fit of our high clouds to observations. A deeper limitation of our results, however, is structural uncertainty in the microphysics scheme – an issue shared by other studies with convection-permitting models that do not explicitly explore structural sensitivity to choice of microphysics scheme. The highly elongated aspect ratio of the channel we have used might raise concerns that domain geometry might artificially constrain convective aggregation in some fundamental way, but *Wing and Cronin* [2016] found that banded aggregation persisted to at an aspect ratio of 16:1 and even 4:1. Lack of rotation might also constrain the ways in which convection can organize, as well as the disruptive influence to convective aggregation imposed by large-scale rotational circulations. It would be useful, albeit much more

expensive due to the larger meridional width needed, to conduct similar simulations with homogeneous thermal forcing but with differential rotation (as in an equatorial beta-channel). Finally, this study has focused exclusively on the Tropics, so we remind the reader that our modeling setup cannot simulate any important extratropical cloud feedbacks, and that our calculations of climate feedbacks should not be compared directly to global-average climate feedbacks from GCMs.

To frame our discussion of the relative influence on climate of changes in aggregation with warming, compared to the mere existence of aggregation, we use a simple model to describe how each effect would manifest as a climate feedback. Previous hypotheses about climate impacts of aggregation have been founded on the notion that one can write the top-of-atmosphere radiation R, as the sum of the net flux in the non-aggregated state, $N(T)$, plus a product of a degree of aggregation, $A(T)$, and a difference in top-of-atmosphere flux between aggregated and non-aggregated states, $B(T)$:

$$R = N(T) + A(T)B(T). \tag{6}$$

For simplicity, consider each of these to be a function of temperature only. The derivative of R with respect to T then gives the total climate feedback λ, which is composed of three terms:

$$\lambda = \frac{dR}{dT} = \frac{dN}{dT} + A\frac{dB}{dT} + B\frac{dA}{dT}. \tag{7}$$

Here, dN/dT is the climate feedback of a non-aggregated state, and the other two terms determine the influence of aggregation on climate sensitivity. If B is large and negative (as suggested by modeling studies [e.g., *Wing and Emanuel*, 2014] but not necessarily observations [e.g., *Tobin et al.*, 2013]) and A increases with warming, then the last term, BdA/dT, gives rise to a strong negative climate feedback, which can be almost arbitrarily strong if convective aggregation switches on only above a certain surface temperature. Previous work by *Khairoutdinov and Emanuel* [2010] and *Mauritsen and Stevens* [2015] has advanced this "change in aggregation with warming" hypothesis as having the greatest potential to lead to a more negative climate feedback. This study, however, points to the mere presence of aggregation as a more modest but likelier means of reducing climate sensitivity – fundamentally via the other aggregation term, AdB/dT, in Eq. 7, which represents a change in the impact of aggregation with warming.

Physically, B might become more negative with warming for two reasons. The first reason is speculative: the positive longwave cloud-top-height feedback may be stronger if there are more high clouds in the basic state. Based on our simulations and on observations, non-aggregated atmospheres seem to have more high clouds than aggregated atmospheres – although the causal reasons for this could relate either directly to humidity through the effects of saturation deficit and cloud lifetime, or indirectly to humidity or temperature profiles through radiatively-driven divergence in clear-sky regions [*Bony et al.*, 2016]. But a second reason why B might become more negative with climate warming is robust: the difference in clear-sky OLR between a moist and dry atmosphere increasingly diverges with warming, in tandem with the rapid strengthening of the water vapor feedback near present tropical surface temperatures [e.g., Figure 4.32 of *Pierrehumbert*, 2010]. As an example of how this translates to a stronger negative climate feedback in an aggregated state, consider moist adiabats with greenhouse gases of solely water vapor and 400 ppmv of CO_2, and prescribed vertically-uniform relative humidity that remains constant with warming. Based on calculations with RRTMG, an atmosphere with 70% RH has a clear-sky longwave feedback of -1.44 W m^2 K^{-1} between 280 and 310 K, whereas an atmosphere with 30% RH has a clear-sky longwave feedback of -2.34 W m^2 K^{-1} over the same temperature range. Comparing a non-aggregated state (with 70% RH everywhere) to a partially aggregated state (where half of the domain remains at 70% RH but the other half dries to 30%) RH would give a clear-sky longwave contribution to $AdB/dT \approx -0.45$ W m^2 K^{-1} – comparable to our estimate above of -0.41 W m^2 K^{-1} for the non-cloud feedback difference between aggregated and non-aggregated states. The importance of relative humidity in dry regions is not a new result; *Pierrehumbert*

[1995] emphasized "the degree of dryness of subsiding regions" as a key factor in regulation of tropical energy balance and global climate. But it is worth reiterating that aggregation can influence climate sensitivity not only by changing with warming, but also by acting across all surface temperatures to dry the atmosphere overall and enhance the dryness of dry regions. Climate impacts of aggregation could occur through a rapid change in degree of aggregation with warming, or through a subtler influence on the distribution of tropical relative humidity that may already hide within the present climate.

A: Calculation of Organization Index, I_{org}

We follow *Tompkins and Semie* [2017] in calculating the organization index I_{org}, as follows:

1. Convective entities are determined by locating connected convective pixels, defined as grid boxes in which the hourly average vertical velocity at 500 hPa is greater than 0.5 m s^{-1}.
2. For each convective entity, the distance from its centroid to its nearest neighbor (d) is computed.
3. The normalized cumulative distribution function (CDF) of nearest neighbor distances is plotted against the theoretical CDF of nearest neighbor distances in a 2-dimensional Poisson point process $\left(1 - \exp\left(-\gamma\pi d^2\right)\right)$ (as in Figure A.1). The parameter γ is estimated as the number of convective entities per unit area in the domain.
4. I_{org} is defined as the area under curve plotted in the previous step.
5. The above is repeated each hour for the entire simulation to obtain I_{org} as a function of time.

A system with random convection would have a curve in Figure A.1 that fell on the 1:1 line, and a value of I_{org} equal to 0.5. Our channel simulations all lie above the 1:1 line in Figure A.1, yielding values of I_{org} greater than 0.5 and indicating aggregated convection.

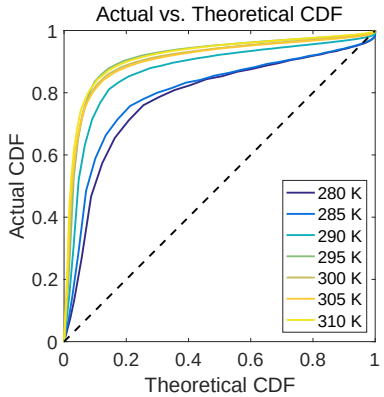

Figure A.1. Empirical cumulative distribution function (CDF) of nearest neighbor distance averaged over days 50-75 plotted against the theoretical CDF of nearest neighbor distance in a Poisson point process. I_{org} is the area under each colored curve.

B: Radiative kernels in RCE

B.1 Radiative kernel methodology

Generating full radiative kernels is time-consuming, as it generally requires calling an offline radiative transfer model for each grid cell and time step with saved vertically-resolved data, in both the longwave and shortwave, for both temperature and specific humidity perturbations, and at each of the n_z model levels in the vertical. Due to the ambiguity introduced by horizontally homogeneous boundary conditions in RCE, and our desire to generate distinct kernels for each surface temperature, we opt for a much less computationally intensive approach that gives approximate kernels. Using saved 3D snapshots at 6-hour intervals between model days 50 and 75, we first sort grid-cell-snapshots by their column relative humidity, $\mathcal{H} = \widehat{q}/\widehat{q^*}$, into N_H bins which each contain an equal number of columns ($N_H = 100$ for results shown in this paper). For each of the N_H bins, we then calculate a composite sounding by averaging temperature, specific humidity, cloud water, and computing cloud fraction at each level for all grid-cell-snapshots in that bin. For each of the N_H composite soundings, we compute a radiative kernel by calculating the sensitivity of both outgoing longwave radiation and absorbed solar radiation to temperature and specific humidity at each model level in the vertical. We use +0.1 K perturbations in temperature and +1% perturbations in specific humidity to compute partial derivatives of the top-of-atmosphere net radiative fluxes. Since 6-hourly output is insufficient to resolve the diurnal cycle, our shortwave radiative transfer calculations use a fixed insolation-weighted zenith angle of 42.2° regardless of time of day, and the solar heating rates are scaled down by a factor 0.408 to reduce the insolation to its time-mean value of 413.6 W m^{-2} [*Cronin*, 2014, note that this is equivalent to using a reduced solar constant of 558 W m^{-2}]. The result of these calculations is eight kernel matrices for each sea-surface temperature – $K_T^{0,L}$, K_T^L, $K_q^{0,L}$, K_q^L, $K_T^{0,S}$, K_T^S, $K_q^{0,S}$, and K_q^S – where a superscript '0' indicates clear-sky (no '0' indicates all-sky), superscripts 'L' and 'S' respectively indicate longwave and shortwave, and subscripts 'T' and 'q' respectively indicate temperature and water vapor kernels. Each kernel matrix is N_H by n_z points. We refer to these kernels as approximate because of the order of averaging: we first create composite soundings for each $\mathcal{H}$ bin, and then calculate kernels, rather than using the more accurate method of calculating kernels for each grid-cell snapshot, then compositing into the appropriate $\mathcal{H}$ bin. Small residuals suggest this approach works adequately, but its performance might suffer if our simulated atmospheres were cloudier.

Before discussing the kernel-based calculation of cloud feedbacks, we describe the radiative kernel for the channel simulation at 300 K (Figure B.1). Combined longwave and shortwave all-sky kernels are plotted, but they are dominated by their longwave components. The temperature profile varies little across $\mathcal{H}$ bins, with largest temperature differences between the moistest and driest regions in and just above the boundary layer, and near the tropopause (Figure B.1a). Variation in relative humidity is largest in the mid-troposphere, with boundary layer drying also evident in the driest 20% of columns, and relative humidities near 10% from 600-900 hPa in the driest columns (Figure B.1b). Contours on Figure B.1b-e show cloud water content (white contours, interval 0.01 g kg^{-1}) and cloud fraction (gray contours, interval 5%), which both increase with $\mathcal{H}$ ranking, and show peaks near the top of the boundary layer and near the tropopause. Strong vertical emissivity gradients show up as local maxima in the temperature kernel, near the boundary layer top in dry regions, along a diffuse upward-sloping line in regions of moderate $\mathcal{H}$ rank that follows the sharp vertical decrease in relative humidity from Figure B.1b, and then near the tops of the optically thick anvil clouds in the moistest regions (Figure B.1c). Below the thick clouds in the moistest regions, sensitivity of top-of-atmosphere net radiation to temperature is very small. The water vapor feedback on top-of-atmosphere radiation is concentrated in the upper troposphere, and to a lesser extent in the moist lower troposphere just above the boundary layer, with reduced feedback in the very dry mid-tropospheric parts of the driest columns (Figure B.1d). Finally, the total temperature plus water vapor kernel is negative everywhere except near the tropopause in the driest regions, with most negative values in and just above the boundary layer in dry regions, and

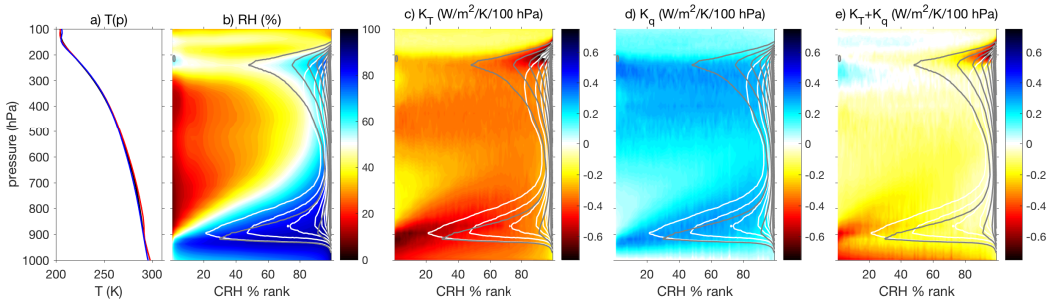

Figure B.1. Radiative kernel for T_S=300 K simulation in long channel geometry. Profiles are binned by column relative humidity, $\mathcal{H}$=$\widehat{q}/\widehat{q^*}$; a) shows the domain-average temperature profile in black, the driest-bin profile in red, and the moistest-bin profile in blue, b) shows the relative humidity as a function of pressure and $\mathcal{H}$ % rank (1=driest column, 100=moistest). c) shows the all-sky temperature kernel, with units of W m^{-2} K^{-1} per 100 hPa of layer mass, and d) shows the all-sky water vapor kernel in the same units W m^{-2} K^{-1} per 100 hPa of layer mass, for water vapor changes at constant relative humidity. e) shows the sum of the temperature and water vapor kernels. Solid gray contours on b)-e) indicate cloud fraction at 5 % increments; solid white contours on b)-e) indicate cloud water content (liquid and ice) at 0.01 g kg^{-1} increments.

around the tops of anvil clouds in moist regions (Figure B.1e). A negative combined temperature and water vapor kernel indicates a stable feedback to temperature changes at constant relative humidity. Our radiative kernels resemble those of both *Feldl et al.* [2017] and *Soden et al.* [2008] (their figures A1 and 1+2, respectively), if our moistest regions are mapped to their equators and our driest regions to their subtropics. The match between our kernels and those of *Feldl et al.* [2017] is closer, however, because they used an aquaplanet with no seasonal cycle, whereas the seasonal cycle and land-ocean contrasts in *Soden et al.* [2008] smear out radiative responses across regions of different column humidities.

B.2 Feedback Decomposition

For calculations of feedbacks between T_S and $T_S + 5$ K, we average the kernels from these two temperatures, and apply this average kernel to the change in temperature and moisture profile in each column relative humidity bin. Using a kernel from two endpoints is similar to the methodology used by *Jonko et al.* [2012], where an average of $1\times CO_2$ and $8\times CO_2$ kernels were used to calculate feedbacks for $4\times CO_2$-$2\times CO_2$ climate changes. As in *Soden et al.* [2008], their equation 25, the cloud feedbacks are given by kernel-corrected changes in CRF in the longwave and shortwave:

$$\lambda^L_{\text{cloud}} = \frac{1}{\Delta T_S}\left[\Delta\text{CRF}^L + (K^{0,L}_T - K^L_T)\Delta T + (K^{0,L}_q - K^L_q)\Delta \log q\right] \quad \text{(B.1)}$$

$$\lambda^S_{\text{cloud}} = \frac{1}{\Delta T_S}\left[\Delta\text{CRF}^S + (K^{0,S}_T - K^S_T)\Delta T + (K^{0,S}_q - K^S_q)\Delta \log q\right] \quad \text{(B.2)}$$

$$\lambda_{\text{cloud}} = \lambda^L_{\text{cloud}} + \lambda^S_{\text{cloud}}. \quad \text{(B.3)}$$

The result of this kernel-based correction is an increase in the cloud longwave feedback, by an average of +0.18 W m^{-2} K^{-1} across all surface temperatures, and a slight decrease in the cloud shortwave feedback, by an average of -0.04 W m^{-2} K^{-1} across all surface temperatures. Including this positive net correction brings the total cloud feedback to +0.25 W m^{-2} K^{-1}, averaged across temperatures, which is on the lower side of what is found in global models [e.g., *Soden and Held*, 2006]. In both the channel simulations and the small-domain simulations, the longwave cloud feedback is generally positive despite a decreasing high cloud fraction with warming. This result is consistent with feedback analysis of GCMs, which shows that

the positive longwave cloud altitude feedback outweighs the negative longwave cloud amount feedback over much of the tropics [*Zelinka et al.*, 2012]. If high cloud tops remained at fixed temperature rather than fixed altitude with surface warming, this positive cloud altitude feedback might simply cancel the total temperature feedback (described below) in the fraction of the sky covered by such clouds, so the cloud/non-cloud partitioning of the longwave feedback in a kernel analysis might depend on the vertical coordinate used.

The kernel approach also allows us to look at how non-cloud feedbacks change with temperature (Figure B.2). We separate the non-cloud feedbacks into Planck, lapse-rate, and water vapor feedbacks; the total temperature feedback is given by the sum of the Planck feedback, or radiative response to a unit of vertically uniform temperature change (vertically uniform stratospheric warming is included here as well), and the lapse-rate feedback, or radiative response to the temperature change that departs from vertical uniformity. Note that these non-cloud feedbacks are calculated with the all-sky kernels, so they include the influence of a background cloud field in increasing or decreasing the sensitivity of top-of-atmosphere fluxes to temperature and humidity, but they include only changes in temperature and humidity fields; they are "non-cloud" in that they do not account for changes in clouds. Figure B.2a shows that with warming, an increasingly positive water vapor feedback (blue) is offset by an increasingly negative lapse-rate feedback (red), leading to a weak positive trend in water vapor plus lapse rate feedbacks (magenta) with surface warming. The countervailing temperature-dependencies of these feedbacks can be explained by the top-heavy vertical warming (Figure B.2b) and moisture change (Figure B.2c) profiles, which are both accentuated for warmer surfaces. The validity of the kernel method can be tested by checking to see whether the sum of the kernel-based feedbacks (including the kernel-corrected cloud feedbacks), sum to the total Cess feedback; the difference between these two quantities is shown in orange symbols in Figure B.2a). Agreement is generally good at low sea-surface temperatures, but the disparity between kernel-estimated feedback and actual radiative feedbacks grow as SST increases, and the magnitude of the residual depends on our model of radiative response to water vapor. We show results in Figure B.2a) with both logarithmic response to water vapor (blue solid line) and linear response to water vapor (blue dash-dotted line):

$$\lambda_q^{\log} = K_q \frac{\Delta \log q}{\Delta T_S} \tag{B.4}$$

$$\lambda_q^{\text{lin}} = K_q \frac{1}{q_0} \frac{\Delta q}{\Delta T_S}. \tag{B.5}$$

These two feedbacks are equivalent in the limit that $\Delta q/q_0$ is small, because then $\Delta q/q_0 \approx \Delta \log q$, but they diverge for $\Delta q/q_0 \sim 1$ and larger, with greater response in the linear model than in the logarithmic one. Figure B.2c shows that the specific humidity response in the mid- and upper-troposphere, especially at warm surface temperatures, is not by any means a small relative perturbation – the mixing ratio in the 310 K SST simulation is as much as *12 times* larger than that in the 305 K simulation, due to large upper-tropospheric temperature changes of nearly 20 K and the strong temperature-dependence of Clausius-Clayperon at low temperatures. The difference between assuming linear versus logarithmic water vapor response in the feedback calculation thus increases with warming, to over 1 W m^{-2} K^{-1} at surface temperatures of 305-310 K. A logarithmic radiative response to water vapor response apparently leads to smaller residuals than a linear radiative response – as was also found by *Feldl et al.* [2017] relative to *Feldl and Roe* [2013b]. An explanation for the near-logarithmic radiative forcing of greenhouse gases, including water vapor, has been recently provided by *Huang and Shahabadi* [2014] as arising from a locally linear temperature profile together with an exponential decay of absorber concentration in height, near the reference-climate emission level.

The Planck feedback is weakly temperature-dependent, increasing in magnitude from -3.4 W m^{-2} K^{-1} for 280-285 K to -4.1 W m^{-2} K^{-1} for 305-310 K. Although the Planck feedback and its temperature-dependence are mostly captured by the simple estimate $\lambda_e = 4\sigma T_e^3$, with $T_e = (\text{OLR}/\sigma)^{1/4}$, the actual Planck feedback is slightly less negative than

this estimate by $\sim$0.2 W m^{-2} K^{-1} (see solid versus dash-dotted black lines in Figure B.2a). Reasons for this small but nonzero deviation will be discussed more in future work.

Acknowledgments

We acknowledge high-performance computing support from Yellowstone [*Computational and Information Systems Laboratory*, 2012] provided by NCAR's Computational and Information Systems Laboratory, sponsored by the National Science Foundation. We thank Associate Editor Chris Bretherton and two anonymous reviewers for comments that helped improve the manuscript. We also thank Sandrine Bony for providing the data from *Bony et al.* [2004], Nicole Feldl for helpful discussion of radiative kernels, and Marat Khairoutdinov for freely providing SAM. Radiative kernels and model configuration files are available at

`https://www.dropbox.com/sh/fz236q5hnt7ksjo/AADebZq7FDmUOMV6UR-43KGpa?dl=0`

, and SAM model output files are available from the authors upon email request (twcronin@mit.edu). TWC was supported by NSF Award AGS-1623218 ("Collaborative Research: Using a Hierarchy of Models to Constrain the Temperature Dependence of Climate Sensitivity"). AAW was supported by an NSF Postdoctoral Research Fellowship Award AGS-1433251. Both authors contributed equally to this work.

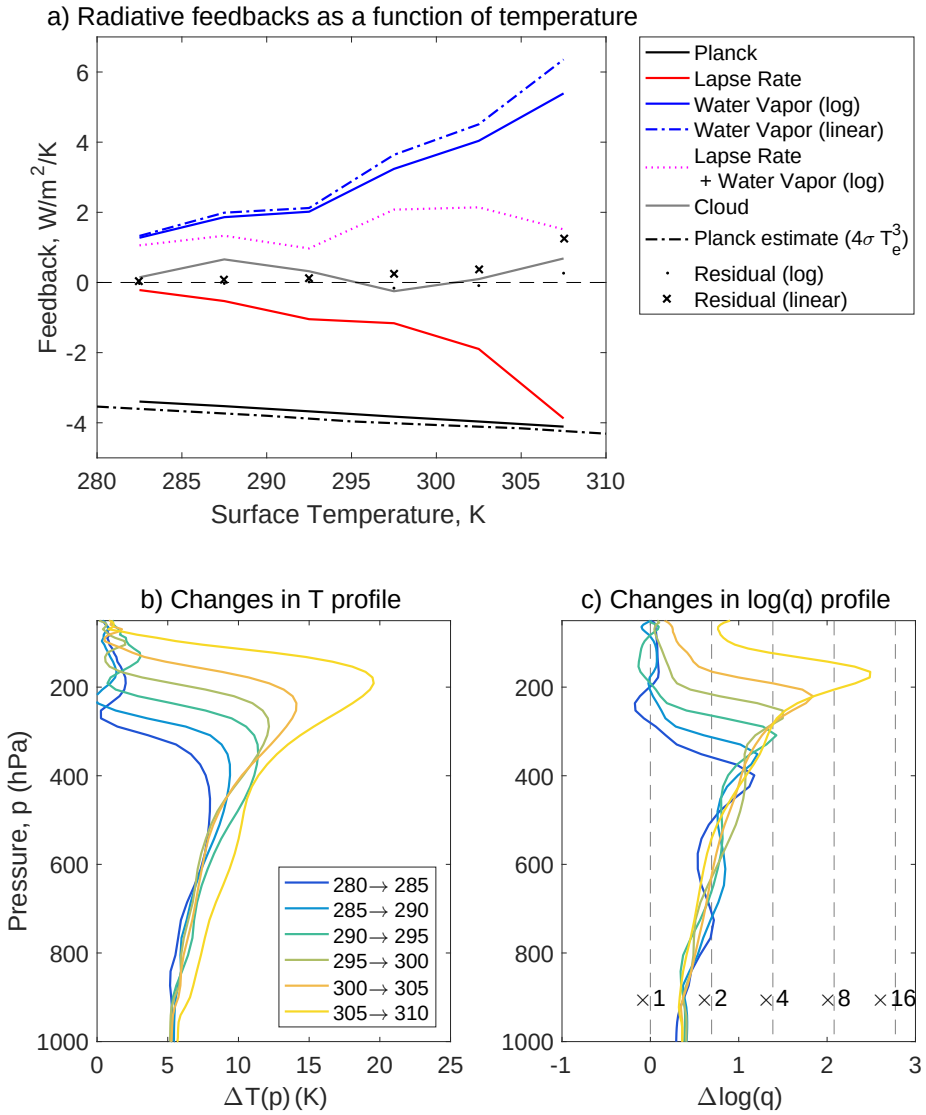

Figure B.2. a) Decomposition of feedbacks in channel simulations using all-sky kernels, together with mean-state changes in b) temperature and c) specific humidity. c) Shows the change in the logarithm of specific humidity, with dashed vertical lines indicating the ratio of specific humidity at $T_S + 5$ relative to T_S.

References

Abbot, D. (2014), Resolved snowball Earth clouds, *J. Climate*, *27*, 4391–4402, doi: 10.1175/JCLI-D-13-00738.1.

Allen, M. R., and W. J. Ingram (2002), Constraints on future changes in climate and the hydrological cycle, *Nature*, *419*, 224–232, doi:10.1038/nature01092.

Becker, T., and B. Stevens (2014), Climate and climate sensitivity to changing CO_2 on an idealized land planet, *Journal of Advances in Modeling Earth Systems*, *6*, 1205–1223, doi: 10.1002/2014MS000369.

Becker, T., B. Stevens, and C. Hohenegger (2017), Imprint of the convective parameterization and sea-surface temperature on large-scale convective self-aggregation, *Journal of Advances in Modeling Earth Systems*, *9*, doi:10.1002/2016MS000865.

Bony, S., J.-L. Dufresne, H. L. Treut, J.-J. Morcrette, and C. Senior (2004), On dynamic and thermodynamic components of cloud changes, *Climate Dynamics*, *22*, 71–86, doi: 10.1007/s00382-003-0369-6.

Bony, S., G. Bellon, D. Klocke, S. Sherwood, S. Fermepin, and S. Denvil (2013), Robust direct effect of carbon dioxide on tropical circulation and regional precipitation, *Nature Geoscience*, *6*, 447–451, doi:10.1038/NGEO1799.

Bony, S., B. Stevens, D. M. W. Frierson, C. Jakob, M. Kageyama, R. Pincus, T. G. Shepherd, S. Sherwood, A. P. Siebesma, A. H. Sobel, M. Watanabe, and M. J. Webb (2015), Clouds, circulation and climate sensitivity, *Nature Geoscience*, *8*, 261–268, doi: 10.1038/NGEO2398.

Bony, S., B. Stevens, D. Coppin, T. Becker, K. A. Reed, A. Voigt, and B. Medeiros (2016), Thermodynamic control of anvil cloud amount, *Proceedings of the National Academy of Sciences*, *113*, 8927–8932, doi:10.1073/pnas.1601472113.

Bretherton, C. S., and M. F. Khairoutdinov (2015), Convective self-aggregation feedbacks in near-global cloud-resolving simulations on an aquaplanet, *Journal of Advances in Modeling Earth Systems*, *7*, 1–23, doi:10.1002/2015MS000499.

Cesana, G., and H. Chepfer (2012), How well do climate models simulate cloud vertical structure? A comparison between CALIPSO-GOCCP satellite observations and CMIP5 models, *Geophys. Res. Lett*, *39*, L20,803, doi:10.1029/2012GL053153.

Cess, R. D., and G. L. Potter (1988), A methodology for understanding and intercomparing atmospheric climate feedback processes in general circulation models, *Journal of Geophysical Research: Atmospheres*, *93*, 8305–8314, doi:10.1029/JD093iD07p08305.

Clough, S. A., M. W. Shephard, E. J. Mlawer, J. S. Delamere, M. J. Iacono, K. Cady-Pereira, S. Boukabara, and P. D. Brown (2005), Atmospheric radiative transfer modeling: A summary of the AER codes, *J. Quant. Spectrosc. Radiat. Transfer*, *91*, 233–244.

Computational, and Information Systems Laboratory (2012), Yellowstone: IBM iDataPlex System (University Community Computing)., Boulder, CO: National Center for Atmospheric Research. http://n2t.net/ark:/85065/d7wd3xhc.

Coppin, D., and S. Bony (2015), Physical mechanisms controlling the initiation of convective self-aggregation in a General Circulation Model, *Journal of Advances in Modeling Earth Systems*, *7*, 2060–2078, doi:10.1002/2015MS000571.

Craig, G., and J. Mack (2013), A coarsening model for self-organization of tropical convection, *Journal of Geophysical Research*, *118*, 8761–8769, doi:10.1002/jgrd.50674.

Cronin, T. W. (2014), On the choice of average solar zenith angle, *Journal of the Atmospheric Sciences*, *71*, 2994–3003, doi:10.1175/JAS-D-13-0392.1.

Emanuel, K. A., A. A. Wing, and E. M. Vincent (2014), Radiative-convective instability, *Journal of Advances in Modeling Earth Systems*, *6*, 75–90.

Feldl, N., and G. H. Roe (2013a), Four perspectives on climate feedbacks, *Geophysical Research Letters*, *40*, 4007–4011, doi:10.1002/grl.50711.

Feldl, N., and G. H. Roe (2013b), The nonlinear and nonlocal nature of climate feedbacks, *Journal of Climate*, *26*, 8289–8304, doi:10.1175/JCLI-D-12-00631.1.

Feldl, N., S. Bordoni, and T. M. Merlis (2017), Coupled high-latitude climate feedbacks and their impact on atmospheric heat transport, *Journal of Climate*, *30*, 190–201, doi: 10.1175/JCLI-D-16-0324.1.

Hartmann, D. L., and K. Larson (2002), An important constraint on tropical cloud-climate feedback, *Geophysical Research Letters*, *29*(20), doi:10.1029/2002GL015835.

Held, I., and B. J. Soden (2006), Robust responses of the hydrological cycle to global warming, *Journal of Climate*, *19*, 5686–5699.

Held, I., M. Zhao, and B. Wyman (2007), Dynamic radiative-convective equilibria using GCM column physics, *Journal of the Atmospheric Sciences*, *64*, 228–238, doi: 10.1175/JAS3825.11.

Held, I. M., R. S. Hemler, and V. Ramaswamy (1993), Radiative-convective equilibrium with explicity two-dimensional moist convection, *J. Atmos. Sci*, *50*, 3909–3927.

Holloway, C. E., and S. J. Woolnough (2016), The sensitivity of convective aggregation to diabatic processes in idealized radiative-convective equilibrium simulations, *Journal of Advances in Modeling Earth Systems*, *8*(1), 166–195, doi:10.1002/2015MS000511.

Holloway, C. E., A. A. Wing, S. Bony, C. Muller, H. Masunaga, T. S. L'Ecuyer, D. D. Turner, and P. Zuidema (2017), Observing convective aggregation, *Surveys in Geophysics*, *this issue*.

Huang, Y., and M. B. Shahabadi (2014), Why logarithmic? a note on the dependence of radiative forcing on gas concentration, *Journal of Geophysical Research: Atmospheres*, *119*, 13,683–13,689, doi:10.1002/2014JD022466.

Huang, Y., X. Tan, and Y. Xia (2016), Inhomogeneous radiative forcing of homogeneous greenhouse gases, *Journal of Geophysical Research: Atmospheres*, *121*, 2780–2789, doi: 10.1002/2015JD024569.

Iacono, M., J. S. Delamere, E. J. Mlawer, M. W. Shephard, S. A. Clough, and W. D. Collins (2008), Radiative forcing by long-lived greenhouse gases: Calculations with the AER radiative transfer models, *Journal of Geophysical Research*, *113*, D13,103, doi: 10.1029/2008JD009944.

Ingram, W. (2010), A very simple model for the water vapour feedback on climate change, *Quarterly Journal of the Royal Meteorological Society*, *136*, 30–40, doi:10.1002/qj.546.

Jeevanjee, N., and D. M. Romps (2016), A simple picture for radiative cooling and precipitation change with warming, model Hierarchies Workshop, World Climate Research Programme, Princeton University, 2-4 November.

Jonko, A. K., K. M. Shell, B. M. Sanderson, and G. Danabasoglu (2012), Climate feedbacks in CCSM3 under changing co_2 forcing. part i: Adapting the kernel technique to feedback calculations for a broad range of forcings, *Journal of Climate*, *25*, 5260–5272, doi:10.1175/JCLI-D-11-00524.1.

Khairoutdinov, M., and K. Emanuel (2010), Aggregated convection and the regulation of tropical climate, *Proceedings of the 29th Conference on Hurricanes and Tropical Meteorology, American Meteorological Society*.

Khairoutdinov, M. F., and D. A. Randall (2003), Cloud resolving modeling of the ARM summer 1997 IOP: Model formulation, results, uncertainties, and sensitivities, *Journal of the Atmospheric Sciences*, *60*, 607–625.

Klein, S., and D. Hartmann (1993), The seasonal cycle of low stratiform clouds, *Journal of Climate*, *6*, 1587–1606.

Knutson, T., and S. Manabe (1995), Time-mean response over the tropical Pacific to increased CO_2 in a coupled atmosphere-ocean model, *Journal of Climate*, *8*, 2181–2199.

Mauritsen, T., and B. Stevens (2015), Missing iris effect as a possible cause of muted hydrological change and high climate sensitivity in models, *Nature Geoscience*, *8*, 346–351, doi:10.1038/ngeo2414.

Merlis, T., and T. Schneider (2011), Changes in zonal surface temperature gradients and walker circulations in a wide range of climates, *Journal of Climate*, *24*, 4757–4768, doi: 10.1175/2011JCLI4042.1.

Mlawer, E. J., S. J. Taubman, P. D. Brown, M. J. Iacono, and S. A. Clough (1997), Radiative transfer for inhomogeneous atmospheres: RRTM, a validated correlated-k model for the longwave, *J. Geophys. Res.*, *102*, 16,663–16,682.

Muller, C. J. (2013), Impact of convective organization on the response of tropical precipitation extremes to warming, *J. Climate*, *26*, 5028–5043, doi:10.1174/JCLI-D-12-00655.1.

Muller, C. J., P. A. O'Gorman, and L. E. Back (2011), Intensification of precipitation extremes with warming in a cloud resolving model, *J. Climate*, *24*, 2784–2800, doi:10.1175/2011JCLI3876.1.

Narenpitak, P., C. S. Bretherton, and M. F. Khairoutdinov (2017), Cloud and circulation feedbacks in a near-global aquaplanet cloud-resolving model, *J. Adv. Model. Earth Syst.*, *9*, 1069—1090, doi:10.1002/2016MS000872.

Pendergrass, A. G., K. A. Reed, and B. Medeiros (2016), The link between extreme precipitation and convective organization in a warming climate: Global radiative-convective equilibrium simulations, *Geophys. Res. Lett.*, *43*(21), 11,445–11,452, doi:10.1002/2016GL071285.

Pierrehumbert, R. (2010), *Principles of Planetary Climate*, Cambridge University Press, Cambridge, UK.

Pierrehumbert, R. T. (1995), Thermostats, radiator fins, and the local runaway greenhouse, *Journal of the Atmospheric Sciences*, *52*, 1784–1806.

Popke, D., B. Stevens, and A. Voigt (2013), Climate and climate change in a radiative-convective equilibrium version of echam6, *Journal of Advances in Modeling Earth Systems*, *5*, 1–14, doi:10.1029/2012MS000191.

Ramaswamy, V., O. Boucher, J. Haigh, D. Hauglustaine, J. Haywood, G. Myhre, T. Nakajima, G. Y. Shi, and S. Solomon (2001), *Climate Change 2001: The Scientific Basis. Contribution of Working Group I to the Third Assessment Report of the Intergovernmental Panel on Climate Change*, chap. Radiative forcing of climate change, Cambridge University Press, Cambridge, United Kingdom and New York, NY, USA.

Reed, K. A., B. Medeiros, J. T. Bacmeister, and P. H. Lauritzen (2015), Global radiative-convective equilibrium in the community atmosphere model, version 5, *Journal of the Atmospheric Sciences*, *72*, 2183–2197, doi:10.1175/JAS-D-14-0268.1.

Romps, D. (2011), Response of tropical precipitation to global warming, *Journal of the Atmospheric Sciences*, *68*, 123–138, doi:10.1175/2010JAS3542.1.

Romps, D. (2014), An analytical model for tropical relative humidity, *Journal of Climate*, *27*, 7432–7449, doi:10.1175/JCLI-D-14-00255.1.

Satoh, M., T. Matsuno, H. Tomita, H. Miura, T. Nasuno, and S. Iga (2008), Nonhydrostatic icosahedral atmospheric model (NICAM) for global cloud resolving simulations, *Journal of Computational Physics*, *227*, 3486–3514, doi:10.1016/j.jcp.2007.02.006.

Satoh, M., T. Ohno, A. Wing, S. Bony, B. Stevens, and K. Reed (2017), RCEMIP: Radiative convective equilibrium model inter-comparison project, 14th Annual Meeting of Asia Oceania Geosciences Society, AOGS, Singapore, 6-11 August 2017.

Seeley, J., and D. Romps (2015), Why does tropical convective available potential energy (cape) increase with warming?, *Geophysical Research Letters*, *42*, 10,429–10,437, doi:10.1002/2015GL066199.

Seeley, J., and D. Romps (2016), Tropical cloud buoyancy is the same in a world with or without ice, *Geophysical Research Letters*, *43*, 3572–3579, doi:10.1002/2016GL068583.

Seeley, J. T., N. Jeevanjee, W. Langhans, and D. M. Romps (2017), A new paradigm for tropical anvil clouds, 21st Conference on Atmospheric and Oceanic Fluid Dynamics, American Meteorological Society, Portland OR, 26-30 June.

Sherwood, S. C., S. Bony, and J.-L. Dufresne (2014), Spread in model climate sensitivity traced to atmospheric convective mixing, *Nature*, *505*, 37–42, doi:10.1038/nature12829.

Silvers, L., B. Stevens, T. Mauritsen, and M. Giorgetta (2016), Radiative-convective equilibrium as a framework for studying the interaction between convection and its large-scale environment, *Journal of Advances in Modeling Earth Systems*, *8*, 1330–1344, doi:10.1002/2016MS000629.

Singh, M., and P. O'Gorman (2013), Influence of entrainment on the thermal stratification in simulations of radiative-convective equilibrium, *Geophys. Res. Lett.*, *40*, 4398–4403, doi: 10.1002/glr.50796.

Singh, M., and P. O'Gorman (2015), Increases in moist-convective updraft velocities with warming in radiative-convective equilibrium, *Q. J. R. Meteorol. Soc.*, *141*, 2828–2838, doi: doi:10.1002/qj.2567.

Singh, M. S., and P. A. O'Gorman (2014), Influence of microphysics on the scaling of precipitation extremes with temperature, *Geophysical Research Letters*, *41*, 1–8, doi: 10.1002/2014GL061222.

Soden, B. J., and I. M. Held (2006), An assessment of climate feedbacks in coupled ocean-atmosphere models, *Journal of Climate*, *19*(14), 3354–3360.

Soden, B. J., I. M. Held, R. Colman, K. M. Shell, J. T. Kiehl, and C. A. Shields (2008), Quantifying climate feedbacks using radiative kernels, *Journal of Climate*, *21*, 3504–3520, doi:10.1175/2007JCLI2110.1.

Stein, T. H. M., C. E. Holloway, I. Tobin, and S. Bony (2017), Observed relationships between cloud vertical structure and convective aggregation over tropical ocean, *Journal of Climate*, *30*, 2187–2207, doi:10.1175/JCLI-D-16-0125.1.

Su, H., J. H. Jiang, J. Teixeira, A. Gettelman, X. Huang, G. Stephens, D. Vane, and V. S. Perun (2011), Comparison of regime-sorted tropical cloud profiles observed by CloudSat with GEOS5 analyses and two general circulation models, *Journal of Geophysical Research*, *116*, D09,104, doi:10.1029/2010JD014971.

Tobin, I., S. Bony, C. E. Holloway, J.-Y. Grandpeix, G. Seze, D. Coppin, S. J. Woolnough, and R. Roca (2013), Does convective aggregation need to be represented in cumulus parameterizations?, *Journal of Advances in Modeling Earth Systems*, *5*, 692–703, doi: 10.1002/jame.20047.

Tompkins, A. M., and A. G. Semie (2017), Organization of tropical convection in low vertical wind shears: Role of updraft entrainment, *J. Adv. Model. Earth Syst.*, *9*, doi: 10.1002/2016MS000802.

Vecchi, G., and B. Soden (2007), Global warming and the weakening of the tropical circulation, *Journal of Climate*, *20*, 4316–4340, doi:10.1175/JCLI4258.1.

Weger, R. C., J. Lee, T. Zhu, and R. M. Welch (1992), Clustering, randomness, and regularity in cloud fields: 1. Theoretical considerations, *Journal of Geophysical Research: Atmospheres*, *97*, 20,519–20,536, doi:10.1029/92JD02038.

Wing, A., and K. Emanuel (2014), Physical mechanisms controlling self-aggregation of convection in idealized numerical modeling simulations, *Journal of Advances in Modeling Earth Systems*, *6*, 59–74, doi:10.1002/2013MS000269.

Wing, A. A. (2014), Physical mechanisms controlling self-aggregation of convection in idealized numerical modeling simulations, Ph.D. thesis, Massachusetts Institute of Technology.

Wing, A. A., and T. W. Cronin (2016), Self aggregation in long channel geometry, *Quarterly Journal of the Royal Meteorological Society*, *142*, 1–15, doi:10.1002/qj.2628.

Wing, A. A., K. Emanuel, C. E. Holloway, and C. Muller (2017), Convectve self-aggregation in numerical simulations: A review, *Surveys in Geophysics*, doi:10.1007/s10712-017-9408-4.

Wofsy, J., and Z. Kuang (2012), Cloud-resolving model simulations and a simple model of an idealized walker cell, *Journal of Climate*, *25*, 8090–8107, doi:10.1175/JCLI-D-11-00692.1.

Zelinka, M., and D. Hartmann (2010), Why is longwave cloud feedback positive?, *J. Geophys. Res.*, *115*, D16,117, doi:10.1029/2010JD013817.

Zelinka, M. D., and D. L. Hartmann (2012), Climate feedbacks and their implications for poleward energy flux changes in a warming climate, *Journal of Climate*, *25*, 608–624, doi: 10.1175/JCLI-D-11-00096.1.

Zelinka, M. D., S. A. Klein, and D. L. Hartmann (2012), Computing and partitioning cloud feedbacks using cloud property histograms. Part II: Attribution to changes in cloud amount, altitude, and optical depth, *Journal of Climate*, *25*, 3736–3754, doi:10.1175/JCLI-D-11-00249.1.

Zhang, M. H., W. Y. Lin, S. A. Klein, J. T. Bacmeister, S. Bony, R. T. Cederwall, A. D. D. Genio, J. J. Hack, N. G. Loeb, U. Lohmann, P. Minnis, I. Musat, R. Pincus, P. Stier, M. J. Suarez, M. J. Webb, J. B. Wu, S. C. Xie, M.-S. Yao, and J. H. Zhang (2005), Comparing clouds and their seasonal variations in 10 atmospheric general circulation models with satellite measurements, *J. Geophys. Res.*, *110*, D15S02, doi:10.1029/2004JD005021.